



저작자표시-비영리-동일조건변경허락 2.0 대한민국

이용자는 아래의 조건을 따르는 경우에 한하여 자유롭게

- 이 저작물을 복제, 배포, 전송, 전시, 공연 및 방송할 수 있습니다.
- 이차적 저작물을 작성할 수 있습니다.

다음과 같은 조건을 따라야 합니다:



저작자표시. 귀하는 원저작자를 표시하여야 합니다.



비영리. 귀하는 이 저작물을 영리 목적으로 이용할 수 없습니다.



동일조건변경허락. 귀하가 이 저작물을 개작, 변형 또는 가공했을 경우에는, 이 저작물과 동일한 이용허락조건하에서만 배포할 수 있습니다.

- 귀하는, 이 저작물의 재이용이나 배포의 경우, 이 저작물에 적용된 이용허락조건을 명확하게 나타내어야 합니다.
- 저작권자로부터 별도의 허가를 받으면 이러한 조건들은 적용되지 않습니다.

저작권법에 따른 이용자의 권리는 위의 내용에 의하여 영향을 받지 않습니다.

이것은 [이용허락규약\(Legal Code\)](#)을 이해하기 쉽게 요약한 것입니다.

[Disclaimer](#)

Thesis for the Degree of Master of Engineering

**Reflectance Normalization of High Resolution Satellite
Employing BRD Components of Wide-Swath Satellite**



by

Sang-II Kim

Department of Spatial Information Engineering

The Graduate School

Pukyong National University

February 2012

**Reflectance Normalization of High Resolution Satellite
Employing BRD Components of Wide-Swath Satellite**
(Wide Swath 위성의 BRD 구성 성분을 이용한 고해상도 위성의
반사도 정규화)

Advisor: Prof. Kyung Soo Han

by

Sang-II Kim

**A thesis submitted in partial fulfillment of the requirements
for the degree of
Master of Engineering**

**in Department of Spatial Information Engineering,
The Graduate School,
Pukyong National University**

February 2012

**Reflectance Normalization of High Resolution Satellite
Employing BRD Components of Wide-Swath Satellite**

A dissertation

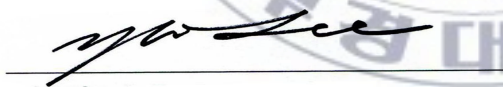
by

Sang-II Kim

Approved by:



(Chairman) Prof. Young Seup Kim



(Member) Prof. Yang Won Lee



(Member) Prof. Kyung Soo Han

February 2012

CONTENTS

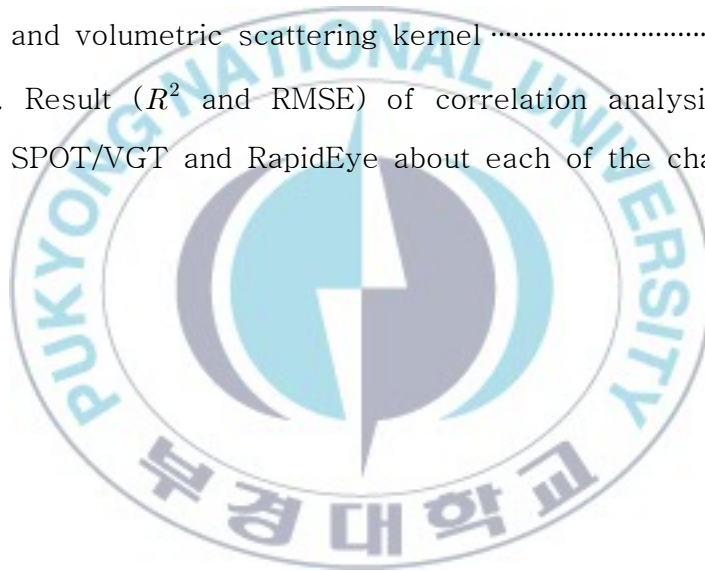
CONTENTS	I
LIST OF TABLES	III
LIST OF FIGURES	IV
ABSTRACT	VIII
1. INTRODUCTION	1
1.1. Problem	1
1.1.1. BRDF (Bidirectional Reflectance Distribution Function) ..	3
1.2. Objectives of this research	4
2. DATA	6
2.1. 1-day images from VGT(vegetation) sensor	7
2.2. 10-day composite images from VEGETATION sensor	8
2.3. Yearly Land Cover from MODIS sensor	9
2.4. RapidEye sensor	11
3. METHODOLOGY	15
3.1. BRDF model	15
3.2. Sample pixel using unsupervised classification	19
3.3. Match up database of SPOT/VGT and RapidEye	23

4. RESULT & ANALYSIS	29
4.1. BRDF model analysis	29
4.2. Sensitivity analysis for solar zenith angle	32
4.3. Sensitivity analysis for viewing zenith angle	36
4.4. Validation results	41
4.4.1. Preliminary validation of SPOT/VGT and RapidEye	41
4.4.2. Comparison BRDF - adjusted weighting	45
5. Conclusions	55
6. REFERENCE	58



LIST OF TABLES

Table 1. Characteristics of SPOT/VGT (VEGETATION) and RapidEye	12
Table 2. The pixel difference of SPOT/VGT and RapidEye	27
Table 3. Input data of RapidEye to estimated geometric kernel and volumetric scattering kernel	42
Table 4. Result (R^2 and RMSE) of correlation analysis between SPOT/VGT and RapidEye about each of the channels	47



LIST OF FIGURES

Figure 1.	The location of study area; left side: Rapideye, right side: SPOT/VGT (VEGETATION)	14
Figure 2.	The schema of method for the retrieval of normalized reflectance by using determined time window with synthetic use SPOT/VGT.	18
Figure 3.	Flow chart for the data processing of BRDF components analysis.	21
Figure 4.	Result of filtering black closed points are selected pixel on forest and grey closed points are selected pixel on cropland; (a) unsupervised classification over the study area; (b) Sample pixel over the study area.	22
Figure 5.	Study area of RapidEye corresponding to 1 pixel of SPOT/VGT; (a) study area of RapidEye; (b) test area of RapidEye.	26
Figure 6.	NDVI validation of SPOT/VGT NDVI and RapidEye NDVI in the study area	27
Figure 7.	Flowchart for the overall data processing of the study	28
Figure 8.	The scatter plot of time series of measured reflectance from 1 January to 31 December 2006; line is reflectance by SPOT/VGT from determined BRDF	

model; (a) b2 band in cropland; (b) b3 band in
cropland; (c) b2 band in forest; (d) b3 band in forest
..... 31

Figure 9. The viewing zenith angle and geometric term (k1f1)
analysis according to the NDVI for (a)–(b) fixed solar
zenith angle 0°, (c)–(d) fixed solar zenith angle 30° and
(e)–(f) fixed solar zenith angle 60° in cropland: (a), (c),
(e) b2 band of the geometric term (k1f1); (b), (d), (f)
b3 band of the geometric term (k1f1). 34

Figure 10. The viewing zenith angle and volumetric term (k2f2)
analysis according to the NDVI for (a)–(b) fixed solar
zenith angle 0°, (c)–(d) fixed solar zenith angle 30° and
(e)–(f) fixed solar zenith angle 60° in cropland: (a), (c),
(e) b2 band of the volumetric term (k2f2); (b), (d), (f)
b3 band of the volumetric term (k2f2). 35

Figure 11. Kernel analysis for fixed viewing zenith angle 0° in
cropland: (a) b2 band of the geometric term (k1f1); (b)
b3 band of the geometric term (k1f1); (c) b2 band of
the volumetric term (k2f2); (d) b3 band of the
volumetric term (k2f2) 38

Figure 12. Kernel analysis for fixed viewing zenith angle 0° in
forest: (a) b2 band of the geometric term (k1f1); (b)
b3 band of the geometric term (k1f1); (c) b2 band of
the volumetric term (k2f2); (d) b3 band of the

	volumetric term (k_2^2)	39
Figure 13.	NDVI based on geometric scattering value (k_1), volumetric scattering value (k_2) of the Band (B2, B3) by the coefficient of reflection: (a) Cropland area; (b) Forest area	40
Figure 14.	Preliminary validation of SPOT/VGT K_0 and RapidEye K_0 in the study area; (a) Red band; (b) Nir band	43
Figure 15.	Preliminary validation of SPOT/VGT K_0 and RapidEye K_0 in the test area; (a) Red band; (b) Nir band	44
Figure 16.	Validation of SPOT/VGT K_0 and RapidEye K_0 -adjusted weighting K_0 in the study area; (a) Red band; (b) Nir band	48
Figure 17.	Validation of SPOT/VGT K_0 and RapidEye K_0 -adjusted weighting K_0 in the test area; (a) Red band; (b) Nir band	49
Figure 18.	Comparisons of SPOT/VGT K_0 and RapidEye K_0 -adjusted weighting K_0 in the studyarea, and test area; (a) Red band; (b) Nir band	50
Figure 19.	K_1 image applied weighting, K_2 image applied weighting and estimated K_0 image over the study area: (a) red band of geometric value; (b) red band of volumetric scattering value; (c) red band of estimated isotropic value; (d) nir band of geometric value; (e) nir band of volumetric scattering value; (f) nir band of	

estimated isotropic value.	52
Figure 20. K1 image applied weighting, K2 image applied weighting and estimated K0 image over the test area: (a) red band of geometric value; (b) red band of volumetric scattering value; (c) red band of estimated isotropic value; (d) nir band of geometric value; (e) nir band of volumetric scattering value; (f) nir band of estimated isotropic value.	54



Wide Swath 위성의 BRD 구성 성분을 이용한 고해상도 위성의 반사도 정규화

김 상 일

부경대학교 대학원 위성정보과학과

요약

지표 변수는 지면 근처의 기후변화에 중요한 역할을 하기 때문에 충분히 정확성이 높은 값들이 산출되어야 한다. BRDF (bidirectional reflectance distribution function) 는 충분한 각도 샘플을 보유하고 있는 wide-swath 위성 데이터를 주로 이용하여 반사도를 정규화한다. 하지만 고해상도 위성은 반경험적인 모델을 적용할 때 narrow swath scanning 때문에 짧은 기간 동안 한 픽셀에 대한 충분한 각도 샘플을 얻기가 불가능하다. 이는 고해상도 위성의 정규화된 반사도를 추론하기 위한 BRDF 모델링을 실행하는데 어려움을 낳는다. 그러므로 본 논문에서는 wide-swath 위성을 이용하여 한반도영역에 대한 BRD 성분의 모수화를 통해 지표반사도의 이방성 효과를 정확하게 진단하고 이해하는 것에 목적이 있으며 또한 고해상도 위성의 정규화된 반사도를 산출하기 위해 kernel based BRDF 모델을 이용하여 직접적으로 해결하는 방안을 고려하였다. 정규화된 반사도인 Isotropic value는 BRDF 변수와 kernel들과 밀접하게 관련되어진다. wide-swath 위성인 SPOT/VGT과 고해상도 위성인 RapidEye의 선형회귀분석 사이의 선형관계는 SPOT/VGT 변수들과 RapidEye의 kernel 값들을 이용하여 수행되어졌다. 또한 회귀모델을 통해 geometric value, volumetric scattering value 그리고 error 항에 대한 가중치 값을 결정하였고 결과적으로 선형회귀분석을 통한 가중치를 적용한 값은 좋은 결과를 도출하였으며 모든 지역에 대하여 SPOT/VGT와 RapidEye의 Isotropic value은 높은 상관관계를 가졌다.

1. INTRODUCTION

1.1. Problem

The land surface reflectance is a key parameter influencing the climate near the surface. Surface albedo is an important parameter of the surface energy budget, and its accurate quantification is of major interest to the global climate modeling community. Therefore, it must be determined with sufficient accuracy for climate change research. As the only energy source, solar radiation plays a fundamental role in determining weather or climate at the atmospheric boundary layer by strong feedback effects (Pokrovsky and Roujean, 2002). This global climate change is undergoing and it is important to exactly understand form and status of surface for monitoring climate change. Consequently, knowledge of the phenology of plant communities is relevant to estimate biological productivity, understanding land-atmosphere interactions and biome dynamics, modeling vegetative inputs into biogeochemical cycles, as well as for the management of vegetation resources (Tarpley et., 1984; Justice et al., 1985). Also, Land surface albedo is defined as the fraction of incident solar irradiance reflected by Earth's surface over the whole solar spectrum (Dickinson, 1983). Especially, wide-swath satellite has anisotropy effects that can cause serious error in estimations of solar radiation

parameters such as reflectance, albedo, vegetation indices(Yeom *et al.*, 2005; Yeom *et al.*, 2009). The anisotropic behavior of surface reflectance is described by the Bidirectional Reflectance Distribution Function (BRDF). In particular, the characteristics of the bidirectional reflectance distribution function (BRDF) when using earth observation system (EOS) are important for normalizing the reflected solar radiation from the earth's surface. The wide swath satellites like SPOT/VGT (VEGETATION) permit sufficient angular sampling, but high resolution satellites are impossible to obtain sufficient angular sampling over a pixel during short period because of their narrow swath scanning and VZA (Viewing Zenith Angle) range within the range 0~5°. Consequently, BRDF parameters are difficult to directly calculate from high resolution satellites. This study estimated reflectance normalization of high-resolution (RapidEye) satellite through the SPOT/VGT BRDF components.

1.1.1. BRDF (Bidirectional Reflectance Distribution Function)

The BRDF can be used to correct reflectance to the reflectance at nadir (Kimes et al., 1985; Roujean et al., 1992). Therefore, the BRDF is one of the most important factors to consider when utilizing satellite data and deriving biophysical information from the ground surface (Chopping, 2000; Wanner & Strahler, 1995). Also, this model has been optimized to base on the wide-swath satellite to provide sufficient angular sampling for a short time. There are several kinds of BRDF models, mainly utilizing physical (Gao, 1993), semi-empirical (Roujean et al., 1992) and empirical (Walthall et al., 1985) methods to estimate standard sun-target-sensor geometry. Various studies related to BRDF have been conducted, including Bidirectional Reflectance Factor (BRF) data measurement (Chopping, 2000; Kimes et al., 1985), retrieval of information from BRDF (Lucht, Schaaf, & Strahler, 2000; Pinty & Verstraete, 1991; Privette, Eck, & Deering, 1997), and BRDF model development (Hu, Wanner, Li, & Strahler, 1997; Lacaze & Roujean, 2001; Roujean et al., 1992; Wanner & Strahler, 1995).

1.2. Objectives of this research

Wide swath satellites like SPOT/VGT can observed reflectance with sufficient angular sampling, but high resolution satellites such KOMPSAT-2, SPOT-4, 5 and RapidEye are very difficult to obtain sufficient angular sampling over a pixel during short period because of their long term revisit period, narrow swath scanning and VZA (Viewing Zenith Angle) range within the range $0\sim5^{\circ}$. Therefore, BRDF parameters are difficult to directly calculate from high resolution satellites. The calculated reflectance values by BRDF model can provide the reflectance property. This thesis contained two goals. First step was an analysis of BRD components. Second step was to estimate normalized reflectance of RapidEye by applying the analysis of BRD components to high resolution image. The objectives of this research involved the following step:

To supply insufficient angular samplings, this study is to add BRDF modeling of high resolution satellites through identifying BRDF components by extracting geometric and volumetric term. Therefore,

we can exactly understand bi-direction effect of surface reflectance that plays an important role to moisture of surface and energy balance. Also, this study performed as the preliminary data for apply to high-resolution satellite. The study can provide exact surface parameters through eliminated BRD effect when calculated biophysical index of plant by BRDF model.

The purpose of this study is to be an efficiency assessment for reflectance normalization of RapidEye employing BRDF components of wide-swath satellite. We used semi-empirical BRDF model to estimated SPOT/VGT BRDF components and reflectance normalization of RapidEye.



2. DATA

This study used VEGETATION sensor data, RapidEye data. The study area of SPOT/VGT (VEGETATION) was a section of Northeast Asia bounded by 32.50–40.0°N and 124.48–130.0°E. RapidEye was a section of KOREA between 35.56–35.98°N and 127.13–127.34°E. The BRDF was estimated over the study period of January 1 to December 31, 2006, and 2009 in the SPOT/VGT. The climate in this area is temperate with four distinct seasons, and includes both continental and oceanic features. Summer is hot and humid whereas winter is snowy and cold. Most heavy rain occurs in summer during the monsoon season while autumn brings dry weather with colder air flowing from the north. Spring weather is generally benign except for occasional Asian dust events. This study used MODIS Land Cover, VEGETATION sensor data, RapidEye data to estimate the Normalized reflectance of high resolution satellite (RapidEye).

2.1. 1-day images from VGT(vegetation) sensor

The VEGETATION (VGT) sensor on board the SPOT-4 platform was launched in March 1998 (<http://spot-vegetation.com>). The instrument observes a region of the Earth 2250 km wide with daily coverage. The satellite has an equatorial local crossing time of 10:30 in the morning local solar time. The across track resolution is approximately 1.1 km at the nadir. The data are projected and interpolated to a constant pixel resolution of approximately one km². Four spectral bands are available: B0 between 0.43 and 0.47 μm (blue), B2 between 0.61 and 0.68 μm (red), B3 between 0.78 and 0.89 μm (near infrared) and SWIR between 1.58 – 1.75 μm (short wave infrared). Daily, surface reflectance (S1) products were used for this study. Also, it is optimized for vegetation observation to one of the representative polar-orbiting satellites. Besides the band, S1 product includes angle data of satellite/sun, composite time, NDVI (Normalized Difference Vegetation Index) and SM (Status Map) data. SM data provides clear, shadow, uncertain and cloud condition to each pixel. When was clear pixel, the study was performed.

2.2. 10-day composite images from VEGETATION sensor

The standard 10-day composite data (S10) are produced and made publicly available (<http://www.free.vgt.vito.be>). There are three VGT products: P, S1 (daily), and S10 (10-day) (Passot, 2000; Jang et al., 2006). We acquired the VGT S10 product for the period January–December 2006. Vegetation indices such as NDVI, fraction of vegetation cover (FVC), and normalized difference water index (NDWI) were calculated for all the 10-day composite images. The temporal compositing method for generating standard S10 images selects the observation with the maximum NDVI value during the 10-day period. Three 10-day composites were available each month: days 1–10, days 11–20, and day 21 to the end of the month (Xiao et al., 2004b).

2.3. Yearly Land Cover from MODIS sensor

The MODIS sensor was launched on NASA's Terra satellite in December 1999. It has a $\pm 55^\circ$ scanning pattern that produces a 2330-km-wide swath from a 705-km polar orbit; Terra crosses the equator southward at about 10:30 local time. This results in global coverage every one to two days (King et al., 1992). Seven of the 36 spectral bands in the MODIS sensor are primarily designed for the study of vegetation and land surfaces: blue (459–479 nm), green (545–565 nm), red (620–270 nm), near infrared (841–875 nm and 1230–1250 nm), and shortwave infrared (1628–1652 nm and 2105–2155 nm). The MODIS Land Cover Type product contains multiple classification schemes, which describe land cover properties derived from observations spanning a year's input of Terra data. The primary land cover scheme identifies 17 land cover classes defined by the International Geosphere Biosphere Programme (IGBP), which includes 11 natural vegetation classes, 3 developed and mosaicked land classes, and three non-vegetated land classes. The MODIS Terra Land Cover Type Yearly L3 Global 1 km SIN Grid product incorporates five different land cover classification schemes, derived through a supervised decision-tree classification method:

- Land Cover Type 1: IGBP global vegetation classification scheme
- Land Cover Type 2: University of Maryland (UMD) scheme

- Land Cover Type 3: MODIS-derived LAI/fPAR scheme
- Land Cover Type 4: MODIS-derived Net Primary Production (NPP) scheme
- Land Cover Type 5: Plant Functional Type (PFT) scheme



2.4. RapidEye sensor

The second sensor used within this study is the multispectral sensor RapidEye. The RapidEye system consists of five satellites that carry the same kind of sensor. The RapidEye sensors have five bands in the spectral range between 400 and 900 nm. The features differentiating the RapidEye system from other multi-spectral sensors are for one the additional band in the red-edge region of the spectrum that allows a better analysis of vegetation, but also the high spatial resolution (5m) and the high repetition rate of 1 to 3 days of the sensors due to RapidEye being a sensor system on five satellites. RapidEye Standard Image Product Processing Levels is RapidEye Ortho Product (3A); Radiometric, sensor and geometric corrections applied to the data. All products have been rectified using a DTED Level 1 SRTM DEM or better, and with appropriate ground control can meet an accuracy of 6m 1-sigma (12.7 m CE90). The highest accuracy achieved by these products will meet 1:25,000 NMAS standards. Table.1 shows a summary of the characteristics of the two satellites. For the analyses presented here, image of each sensor was used. For VGT, the images were acquired on 1 January to 31 December 2010, for RapidEye, the image was acquired on September 30th 2010. The study site is a section of Korea between 32.5° and 40.0°N and 124.5° and 130.0°E in SPOT/VGT. Study area of RapidEye is shown in Figure.1. NDVI is the most widely used vegetation index

in order to uncover biological characteristics of vegetation canopy (Jiang et al., 2006). NDVI is a useful index to monitoring growth of the vegetation cover. NDVI can calculate using the reflectance difference of RED channel (B2) and NIR channel (B3) which is maximum surface vegetation chlorophyll. Therefore, this study was performed by B2 and B3 band which are useful for monitoring in growth of vegetation cover.



Table 1. Characteristics of SPOT/VGT(VEGETATION) and RapidEye.

Mission characteristic	Information	
	SPOT/VGT	RapidEye
Orbit	820km in	630 km in
Altitude	Sun-synchronous orbit	Sun-synchronous orbit
Spectral Bands	Capable of capturing any of the following spectral bands:	
Name	Spectral Bands (nm)	Spectral Bands (nm)
Blue	430 – 470	440 – 510
Green		520 – 590
Red	610 – 680	630 – 685
Red Edge		690 – 730
NIR	780 – 890	760 – 850
SWIR	1580 – 1750	
Pixel size	1km	5m

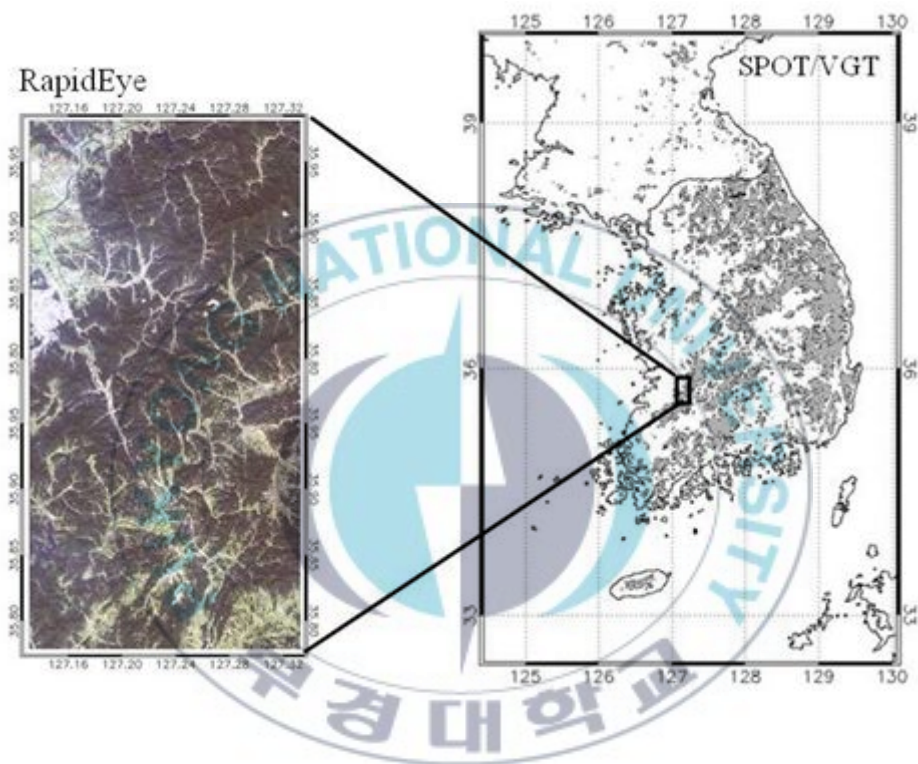


Figure 1. The location of study area; left side: Rapideye, right side: SPOT/VGT (VEGETATION)

3. METHODOLOGY

3.1. BRDF model

Procedure for correction the angle effects of surface depend on the BRDF. In addition, it is essential to estimate accurate reflectance through BRDF. In particular, Kernel-driven semi-empirical models can solve complex relationships to be in estimating BRDF. We used the method developed by Roujean, Leroy, and Deschamps (1992), considered to be the basic form for semi-empirical BRDF models, to simulate the BRDF parameters:

$$\rho(\theta_s, \theta_v, \phi) = k_0 + k_1 f_1(\theta_s, \theta_v, \phi) + k_2 f_2(\theta_s, \theta_v, \phi) \quad (1)$$

$$f_1(\theta_s, \theta_v, \phi) = \frac{1}{2\pi} [(\pi - \phi) \cos \phi + \sin \phi] \quad (2)$$
$$\times \tan \theta_s \tan \theta_v - \frac{1}{\pi} (\tan \theta_s + \tan \theta_v$$
$$+ \sqrt{\tan^2 \theta_s \tan^2 \theta_v - 2 \tan \theta_s \tan \theta_v \cos \phi})$$

$$f_2(\theta_s, \theta_v, \phi) = \frac{4}{3\pi} \frac{1}{\cos \theta_s + \cos \theta_v} \quad (3)$$
$$\times \left[\left(\frac{\pi}{2} - \xi \right) \cos \xi + \sin \xi \right] - \frac{1}{3}$$

where

ξ : phase or scattering angle

$$\cos \xi = \cos \theta_s \cos \theta_v + \sin \theta_s \sin \theta_v \cos \phi$$

where ρ denotes the reflectance in a given spectral channel. The f_1 and f_2 are two angular kernels that depend on the solar zenith angle θ_s , the viewing satellite zenith angle θ_v , and the relative azimuth angle ϕ between the sun and view directions. The term K_0 (isotropic value) stands for the Lambertian coefficient of the model isotropic component. The two other terms K_1 (geometric value) and K_2 (volume scattering value) are coefficients indicative of the relative contributions of f_1 and f_2 , which represent, respectively, the geometric and the volume scattering effects. The three coefficients are retrieved for each channel on a pixel-per-pixel basis adjusting the model of Eq. (1) against VGT measurements in a least square sense. In practice, it is necessary to select extended temporal windows around a period during which land properties are stationary in order to get at least four cloud-free scenes. We consider sets of observations comprised within a 30-day period to retrieve the model coefficients. The results are assigned to the date centred on the 30-day period. The process is repeated with sliding periods of 10 days delineating the composite

frame in order to enhance the temporal sampling (Figure 2). The method was proven to be efficient with time series of AVHRR data (Csiszar et al., 2001; Leroy & Roujean, 1994), which provides a similar angular resolution to VGT (Duchemin & Maisongrande, 2002). Note that the surface BRDF correction is not achieved under turbid conditions for sky illumination.



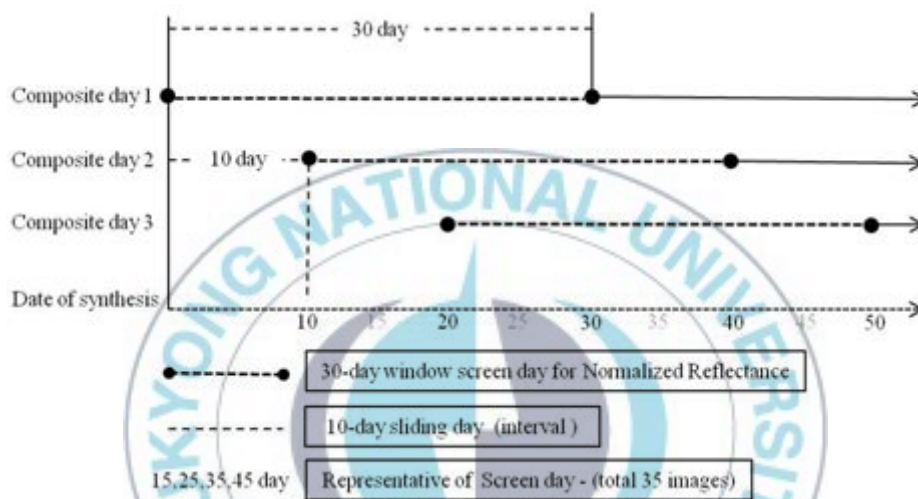
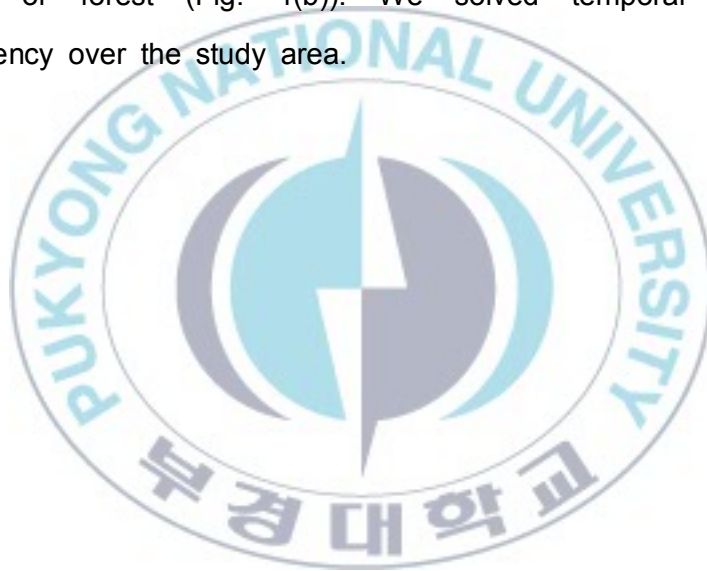


Figure 2. The schema of method for the retrieval of normalized reflectance by using determined time window with synthetic use SPOT/VGT.

3.2. Sample pixel using unsupervised classification

Flow chart for the data processing of BRDF components analysis shown in Figure 3. This study set cropland and forest area, through unsupervised classification of S10 NDVI data. It may be detailed method as follows. In order to generate classified a multi-temporal image products generated using each of these image fusion techniques, an unsupervised classification procedure using the K-means clustering algorithm was widely used. The techniques aforementioned in the previous section are using an unsupervised procedure based on the K-means clustering algorithm (Hartigan and Wong, 1979). The examination carries on the clusters generated from the spectral characteristics of the normalized imagery (Jensen, 1995). In this way, each cluster is statistically separable. This method uses minimum distance criteria and resembles the k-nearest-neighbour rule method. The requirement for clusters classification by distance functions is that the pattern classes tend to have clustering properties. The k-means algorithm is based on the minimization of a performance index, which is defined as the sum of the squared distances from all points in a cluster domain to the cluster center, a Euclidian distance. K-means clustering allocates each pixel to one of k groups or clusters to minimize the within-cluster sum of square. In this case, the total sums of squares, within each cluster is computed as the sum of the centered sum of squares over all non-missing values of each of the

variable. Then, the labeling of cluster was carried out considering prior knowledge and the confusion matrix with MODIS global land cover database. First step distributed 17 clusters considering a number of classes of MODIS Global Land Cover. Fig. 4 is cropland and forest of correspond class. This study in order to adjust temporal or spatial inconsistency of S1 and S10 data extracted sample pixel of correspond area, if all 5×5 pixel would satisfy 25 pixel when is cropland or forest (Fig. 4(b)). We solved temporal or spatial inconsistency over the study area.



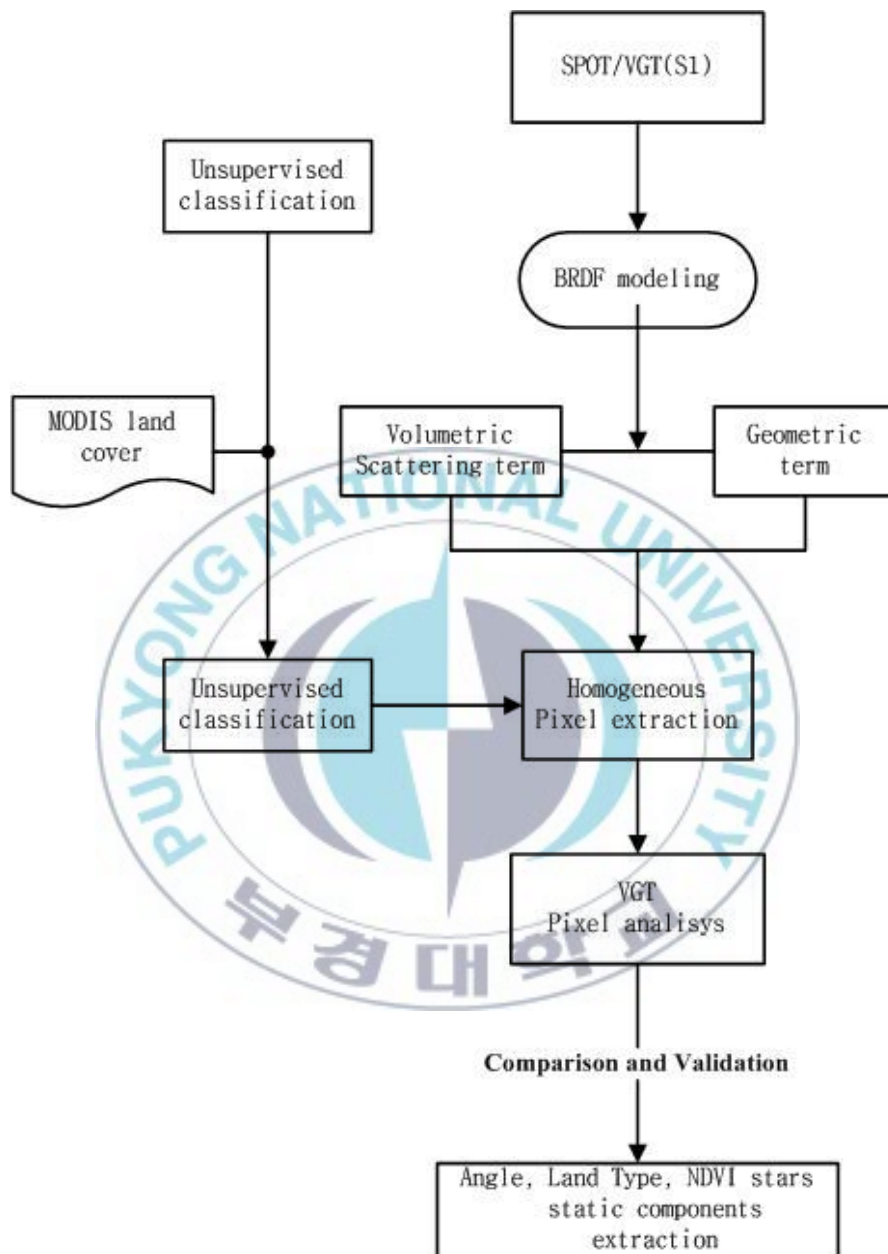


Figure 3. Flow chart for the data processing of BRDF components analysis.

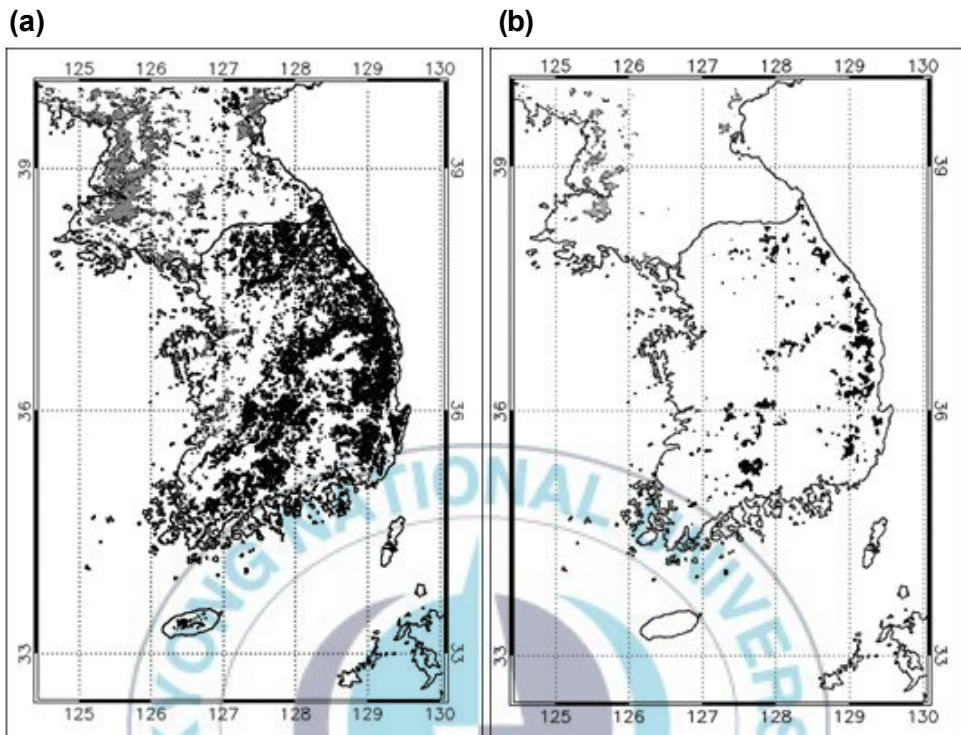


Figure 4. Result of filtering black closed points are selected pixel on forest and grey closed points are selected pixel on cropland; (a) unsupervised classification over the study area; (b) Sample pixel over the study area.

3.3. Match up database of SPOT/VGT and RapidEye

To resolve the pixel difference of SPOT / VGT and Rapid Eye, we fitted pixel size of RapidEye to SPOT/VGT. Figure 5 shows RapidEye site corresponding to 1 pixel of SPOT/VGT. To solve the inconsistency between temporal and spatial patterns, RapidEye has been an average of reflectance values which is 200×200 pixel for fitting SPOT/VGT one pixel (Table 2). Also, relatively large values to standard deviation were excluded. Because of relatively much more one pixel of RapidEye than one pixel of SPOT/VGT, research was intended for broaden forest area than various land surface. Add to that, forest structure is an important factor in the estimation of energy and carbon fluxes between land and atmosphere and is required by modelers regional and global scales (Zhuosen Wang et al., 2011). Also, R^2 considering correlation diagram through distribution of NDVI values corresponding to RapidEye area is 0.62. R^2 seems to be fair on value when compared temporal and spatial differences between the two satellites (Figure 6). The wide swath satellites like SPOT/VGT (VEGETATION) permit sufficient angular sampling, but high resolution satellites such as IKONOS, Quickbird, and KOMPSAT-2 are impossible to obtain sufficient angular sampling over a pixel during short period because of their narrow swath scanning and VZA (Viewing Zenith Angle) range within the range from 0° to 5° degree. Consequently, in

case of semi-empirical BRDF model, it is difficult to parameterize kernel parameters by using high resolution satellites.

$$K_{0\text{ RapidEye}} = \rho_{\text{RapidEye}} - K_{1\text{ SPOT/VGT}} f_{1\text{ RapidEye}} - K_{2\text{ SPOT/VGT}} f_{2\text{ RapidEye}} \quad (5)$$

$$K_{0\text{ RapidEye}} - \rho_{\text{RapidEye}} = -K_{1\text{ SPOT/VGT}} f_{1\text{ RapidEye}} - K_{2\text{ SPOT/VGT}} f_{2\text{ RapidEye}} \quad (6)$$

$$K_{0\text{ RapidEye}} = \rho_{\text{RapidEye}} - a_1 K_{1\text{ SPOT/VGT}} f_{1\text{ RapidEye}} - a_2 K_{2\text{ SPOT/VGT}} f_{2\text{ RapidEye}} + a_0 \quad (7)$$

$K_{0\text{ RapidEye}}$ is normalized reflectance at RapidEye for specific angle condition, $K_{0\text{ SPOT/VGT}}$ is normalized reflectance at SPOT/VGT for specific angle condition.

Each term means following description:

ρ_{RapidEye} - denotes the reflectance of RapidEye in a given spectral channel

$f_{1\text{ RapidEye}}, f_{2\text{ RapidEye}}$ - two angular kernels of BRDF model (depend

on the solar zenith angle θ_s , the viewing satellite zenith angle θ_v , and the relative azimuth angle ϕ between the sun and view directions)

$K_{1SPOT/VGT}$, $K_{2SPOT/VGT}$ - coefficients indicative of the relative contributions of kernel (geometric and volumetric scattering effects of SPOT/VGT)

Therefore, $K_{0RapidEye}$ is estimated by using the Eq. (5). We compared the $K_{0SPOT/VGT}$ and the estimated $K_{0RapidEye}$ by Eq. (5). SPOT/VGT kernels segregated proper kernel to be division and RapidEye kernels computed. We set $K_{0RapidEye} - \rho_{RapidEye}$, $-K_{1SPOT/VGT}f_{1RapidEye}$ and $-K_{2SPOT/VGT}f_{2RapidEye}$ terms corresponding to each channel (Red, NIR band) through Eq. (6); $K_{0RapidEye} - \rho_{RapidEye}$ term as a dependent variable and $-K_{1SPOT/VGT}f_{1RapidEye}$ term, $-K_{2SPOT/VGT}f_{2RapidEye}$ term as the independent variables. Linear regression analysis was performed by using the parameters of SPOT/VGT like as isotropic value ($K_{0SPOT/VGT}$), geometric value ($K_{1SPOT/VGT}$) and volumetric scattering value ($K_{2SPOT/VGT}$), and the kernel values of RapidEye such as geometric kernel ($f_{1RapidEye}$) and volumetric scattering kernel ($f_{2RapidEye}$). Also it made a decision of weighting for K1, K2 and error through regression models. Expression applied weight in each of the channels

is shown in Eq. 7. The overall research method show in Figure 7.

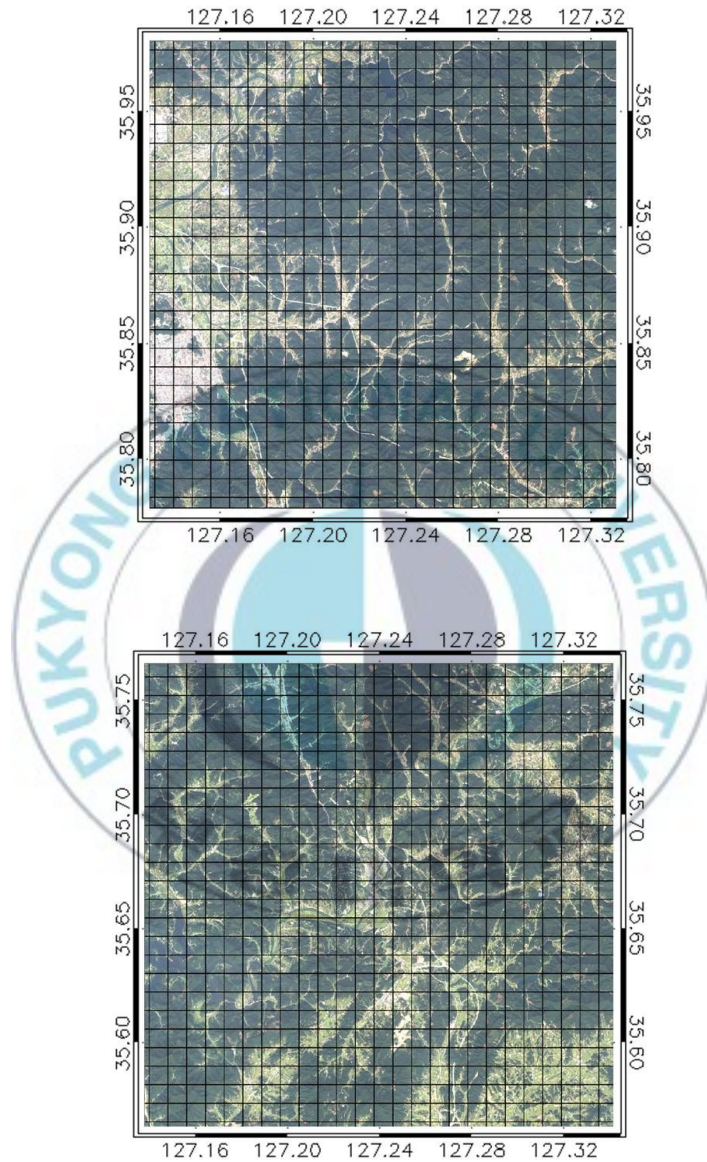


Figure 5. Study area of RapidEye corresponding to 1 pixel of SPOT/VGT; (a) study area of RapidEye; (b) test area of RapidEye.

Table 2. The pixel difference of SPOT/VGT and RapidEye.

	RapidEye	SPOT/VGT
Pixel size	5m	1km
RapidEye of 200 by 200 Pixel = SPOT/VGT 1 by 1 Pixel		

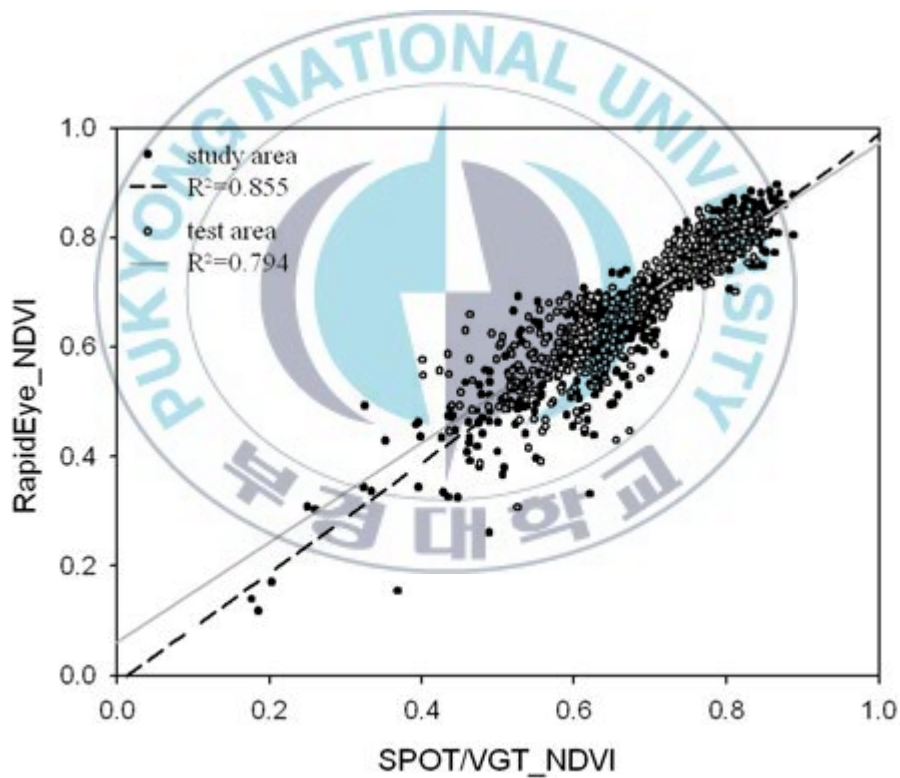


Figure 6. NDVI validation of SPOT/VGT NDVI and RapidEye NDVI in the study area

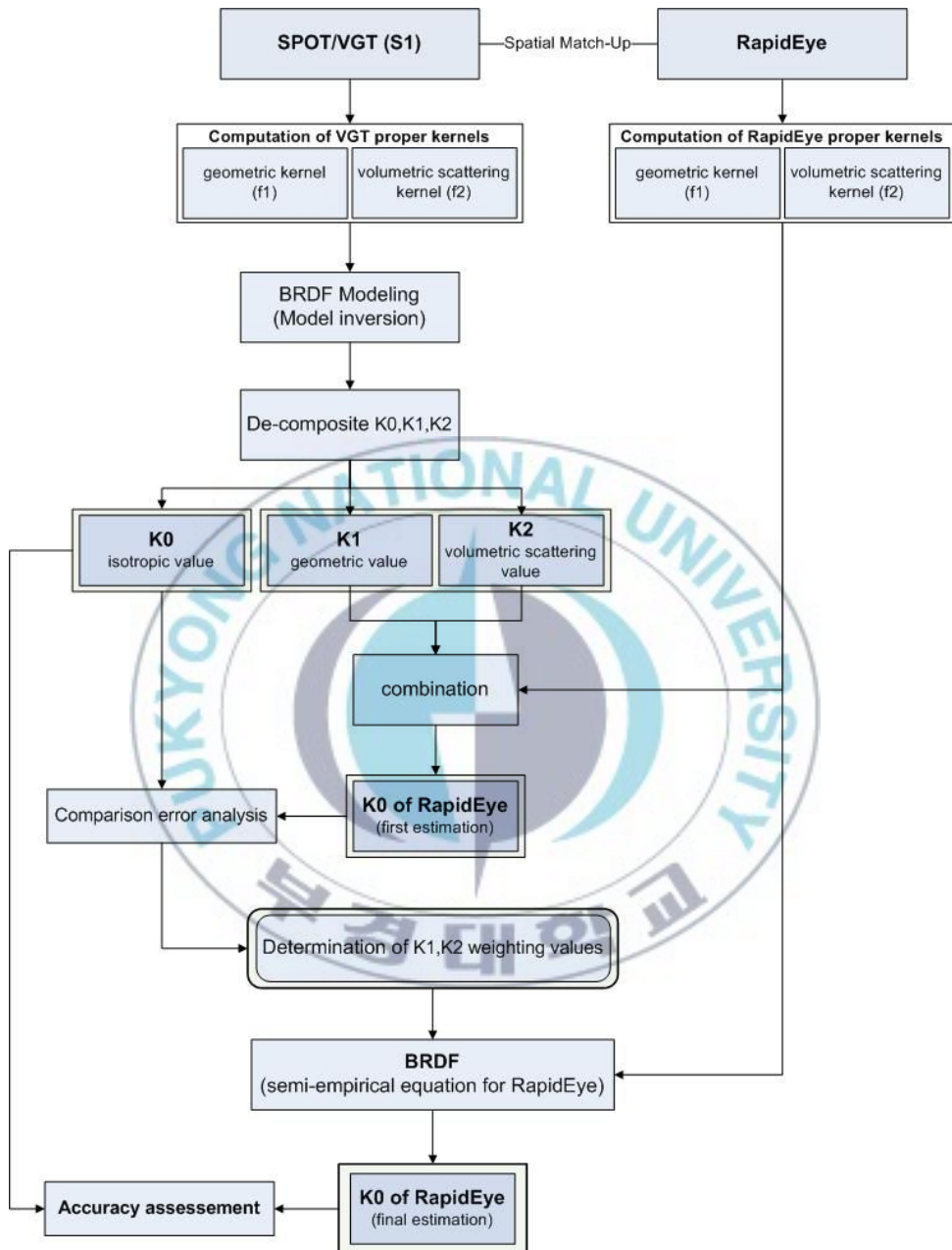


Figure 7. Flowchart for the overall data processing of the study

4. RESULT & ANALYSIS

4.1. BRDF model analysis

K_0 is isotropic component as normalized reflectance on semi-empirical BRDF model of Eq.1. Also, the surface reflectance may then be view as a combination of two different components representative of these two different bidirectional signatures (Roujean et al., 1992). First is component of diffuse reflection by material surface, of reflectance geometric (K_1f_1) term, which takes into account the geometrical structure of opaque reflectors and showing effects. Second is a components of volume scattering, of reflectance volumetric (K_2f_2) term , where the medium is modeled as a collection of randomly located facets absorbing and scattering radiation. Fig. 8 shows a scatter plot of measured and modeled reflectance from 1 January to 31 December 2006 over study area. The red line represents isotropic component (K_0) from the semi-empirical model, whereas the scattered dots show individual values of observed reflectance from the SPOT/VGT visible (red) and NIR channel data. When BRD effects are not eliminated, reflectance is scattered randomly over the year. It is difficult to determine the representative temporal variation without consulting other information and it is difficult to classify reflectance characteristic of surface changing according to the season. Because the values of

geometric and volumetric term are not so great the influence of, represents with the isotropic reflectance value of Lambertian surface. Especially when is cropland, measured reflectance value and isotropic component value by model did correspond to tendency (Figure 8. (a),(b)), and Figure 8. (c),(d) had a generally similar tendency. The geometric and volumetric term occupied a part of the isotropic component value. Also, it known effect of geometric and volumetric term to be greater when is forest than cropland. However, measured reflectance value and isotropic component value was known to be quantitatively match.



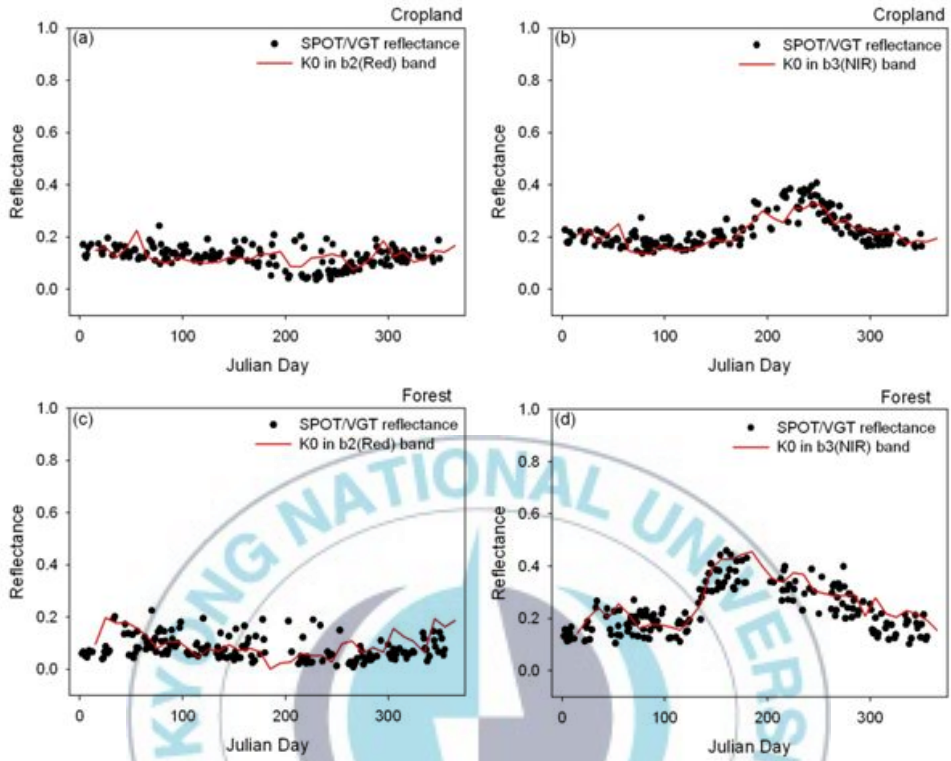
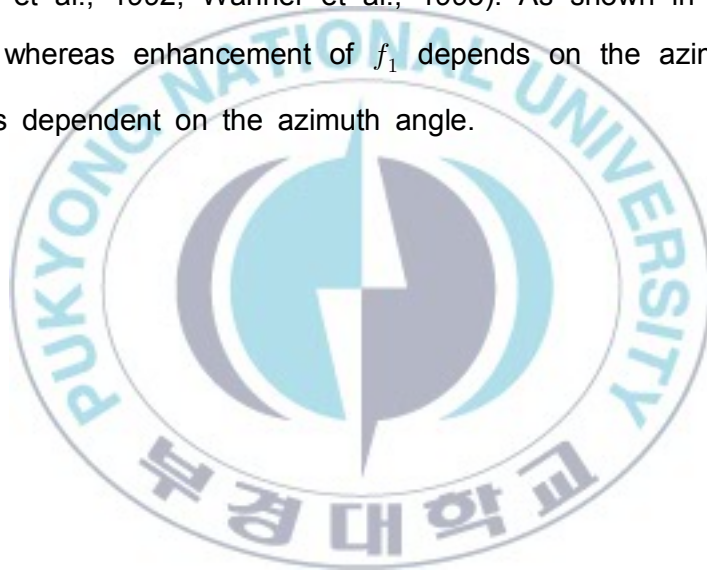


Figure 8. The scatter plot of time series of measured reflectance from 1 January to 31 December 2006; line is reflectance by SPOT/VGT from determined BRDF model; (a) b2 band in cropland; (b) b3 band in cropland; (c) b2 band in forest; (d) b3 band in forest

4.2. Sensitivity analysis for solar zenith angle

As mentioned earlier, wide-swath satellite needs multiple observation values, in order to obtain K_0 , K_1 , K_2 , corresponding same point during the short period. In this study, normalized reflectance during a 30-day window at 10-day composite frame was calculated by each of channel, we produced 36 data. The f_1 , f_2 kernels calculated using the Eq. 2 and Eq. 3. Finally, we estimated geometric and volumetric term. Fig. 9 analyzed sensitivity of solar zenith angle according to geometric term. Solar zenith angle fixed 3 angles (0° , 30° , 60°) and NDVI value (0.125, 0.325, 0.625) and relative azimuth angle (0, 50, 120) set up the fixed values. This study analyzed about B2 and B3 band in cropland. Fig. 9 should not relatively have too much relative azimuth angle. Especially, 0° was not at all impact for relative azimuth angle. But relative azimuth angle effects, as solar zenith angle increase, have an effect on geometric term. As NDVI increase, slope of geometric term shows an increasing tendency. Such as Fig. 9, Fig. 10 analyzed sensitivity of solar zenith angle according to volumetric term. It is divided by fixed 3 Solar zenith angles, we analyzed B2 and B3 band according to the NDVI value. Fig. 10 was not affected about the relative azimuth. As solar zenith angle increase than Fig. 9, the effect of relative azimuth angle and NDVI values was relatively low. To difference distribution according to the sample angles, because the

geometric scattering kernels are governed by the emergence and disappearance of shadows in a discrete opaque canopy, with reflectance decreasing as the sensor direction moves away from the solar direction. The volume scattering kernels, on the other hand, are governed by the phase or scattering angle and the homogeneous medium composed of randomly distributed scattering plane facets, leading to increased reflectance as the zenith angle increases (Roujean et al., 1992; Wanner et al., 1995). As shown in Fig. 9 and Fig. 10, whereas enhancement of f_1 depends on the azimuth angle, f_2 is less dependent on the azimuth angle.



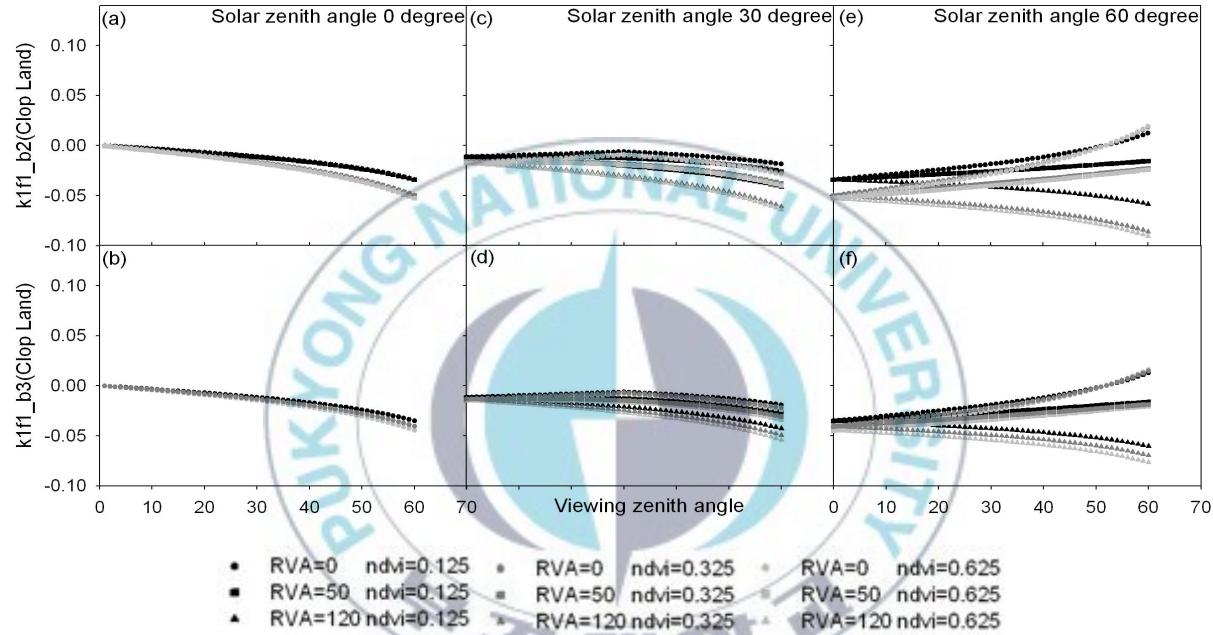


Figure 9. the viewing zenith angle and geometric term (k1f1) analysis according to the NDVI for (a)-(b) fixed solar zenith angle 0°, (c)-(d) fixed solar zenith angle 30° and (e)-(f) fixed solar zenith angle 60° in cropland: (a), (c), (e) b2 band of the geometric term (k1f1); (b), (d), (f) b3 band of the geometric term (k1f1).

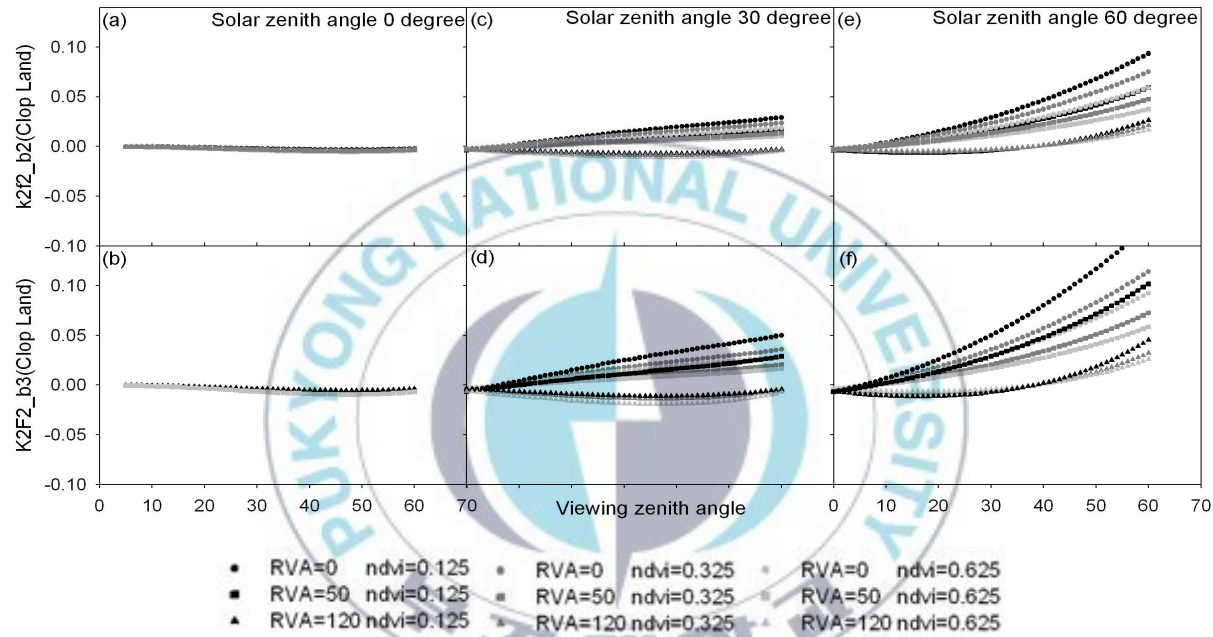


Figure 10. The viewing zenith angle and volumetric term ($k2f2$) analysis according to the NDVI for (a)-(b) fixed solar zenith angle 0° , (c)-(d) fixed solar zenith angle 30° and (e)-(f) fixed solar zenith angle 60° in cropland: (a), (c), (e) b2 band of the volumetric term ($k2f2$); (b), (d), (f) b3 band of the volumetric term ($k2f2$).

4.3. Sensitivity analysis for viewing zenith angle

Solar zenith angle distributes the range of $0^{\circ}\sim 5^{\circ}$ because high resolution satellite is difficult to obtain sufficient angular sampling in short time as time series. To apply future this study such as Fig. 9 and Fig. 10, we performed analysis that is solar zenith angle, geometric and volumetric term when observed nadir on the static part according to the NDVI change. In addition, it was not considered effect about relative azimuth angle. Fig. 11 and Fig. 12 using the fixed viewing zenith angle ($VZA=0^{\circ}$) appeared geometric and volumetric term changes about solar zenith angle, NDVI changes. Fig. 11(a)-(b) shows decreasing tendency about solar zenith angle and geometric term according to the NDVI increase, slope was increased. The difference of bands did not show a clear tendency. Volumetric term was constantly decreased until 50° (solar zenith angle) in Fig. 11(c)-(d) after it showed increasing tendency. B3 band (Fig. 11(d)) appeared a more variety of value distribution than B2 band (Fig. 11(c)). The forest showed the wider distribution of value than cropland (Fig. 12). It was similar overall tendency. When was carried out comparison by land type, forest showed relatively larger value of geometric term than cropland (Fig. 12). In other words, it was shown close relation about angle and NDVI value. Fig. 13 shows the reflectance coefficient of, by NDVI in cropland and forest. In case of in cropland, the change of reflectance coefficient by band could not be almost confirmed (Fig.

13(a)). However, in case of, the reflectance coefficient by band was difference according to the range of NDVI. Forest also showed tendency of similar distribution. NDVI above 0.6 showed similarity that is the increasing B3 band values over the cropland and forest.



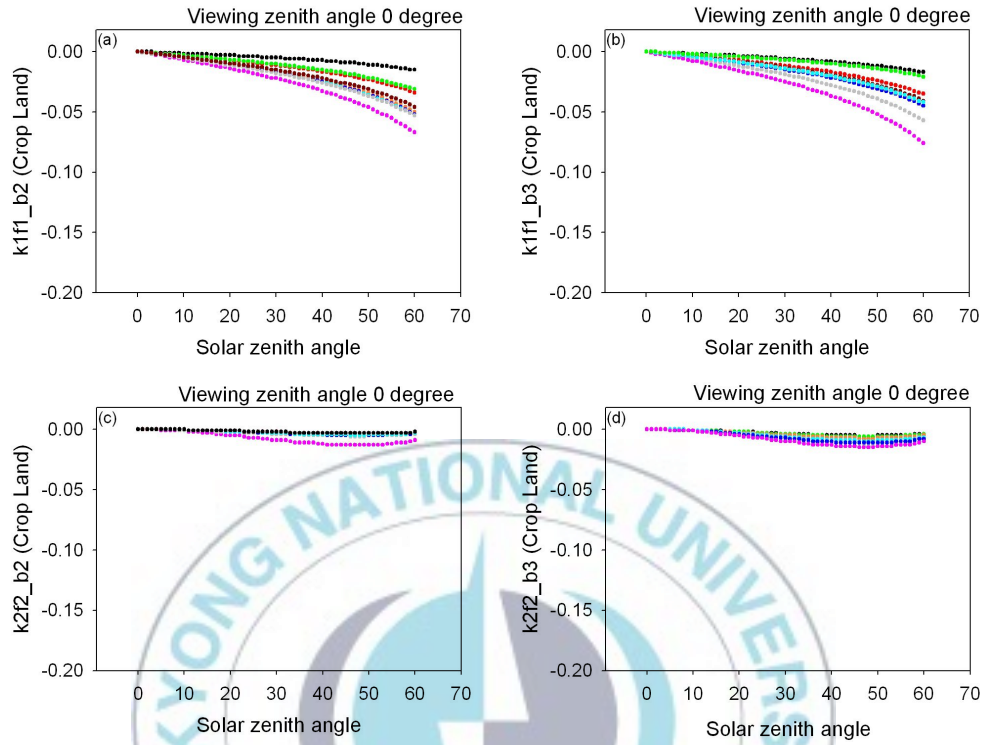


Figure 11. Kernel analysis for fixed viewing zenith angle 0° in cropland: (a) b2 band of the geometric term ($k1f1$); (b) b3 band of the geometric term ($k1f1$); (c) b2 band of the volumetric term ($k2f2$); (d) b3 band of the volumetric term ($k2f2$)

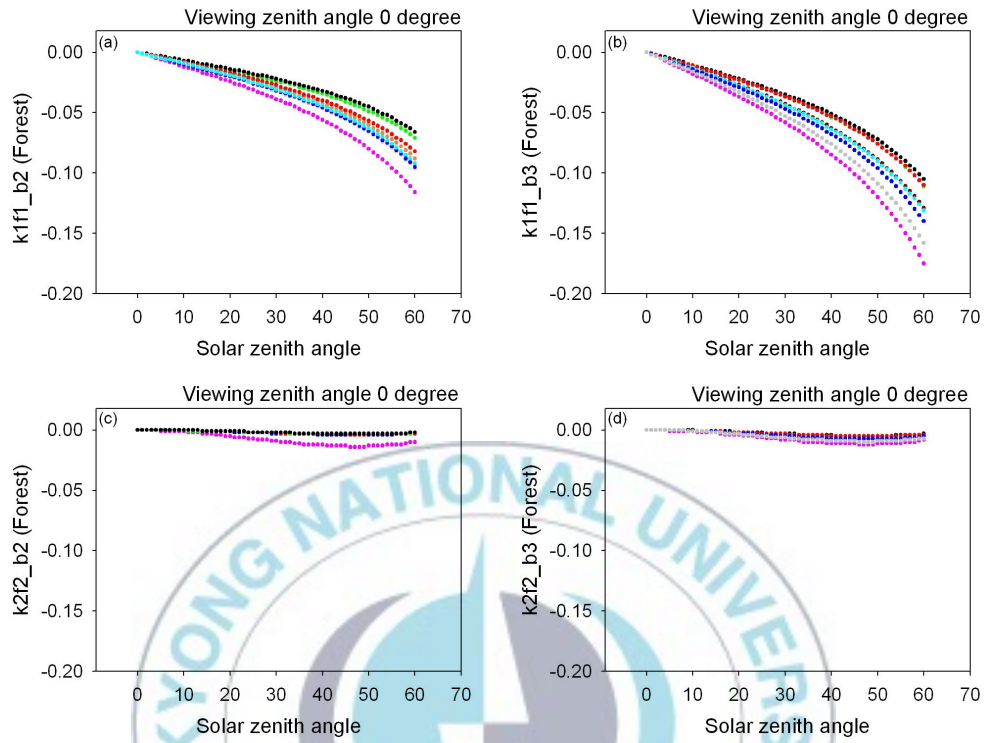


Figure 12. Kernel analysis for fixed viewing zenith angle 0° in forest: (a) b2 band of the geometric term ($k1f1$); (b) b3 band of the geometric term ($k1f1$); (c) b2 band of the volumetric term ($k2f2$); (d) b3 band of the volumetric term ($k2f2$)

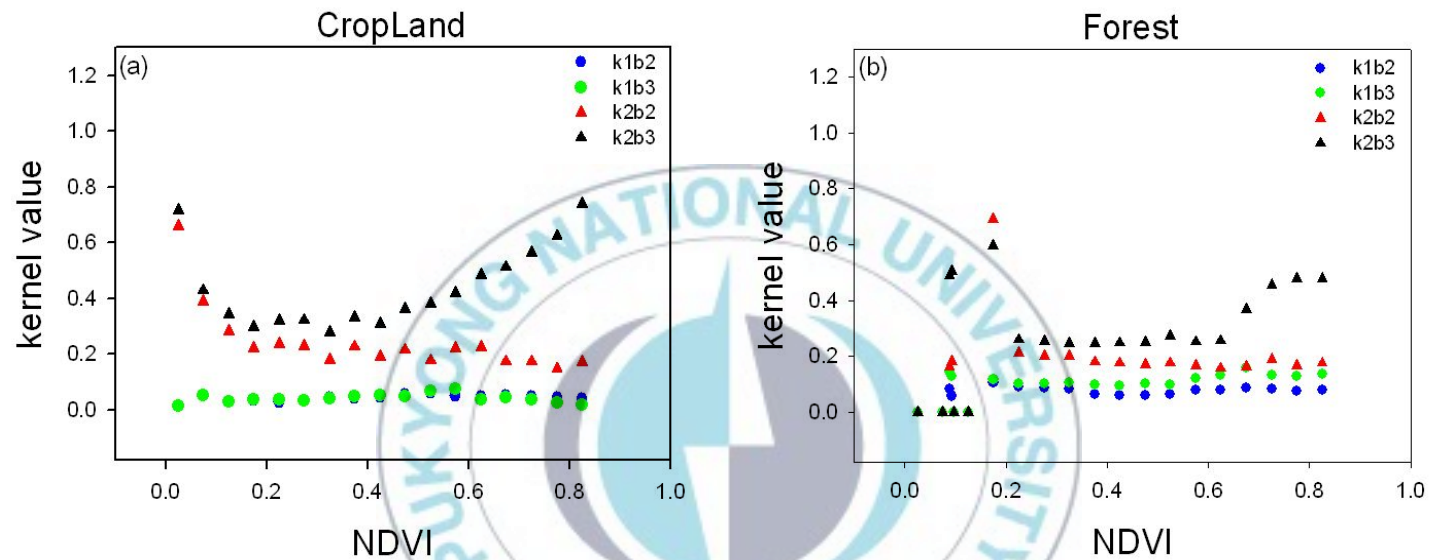


Figure 13. NDVI based on geometric scattering value (k1), volumetric scattering value (k2) of the Band (B2, B3) by the coefficient of reflection: (a) Cropland area; (b) Forest area

4.4. Validation results

4.4.1. Preliminary validation of SPOT/VGT and RapidEye

Two clear-sky RapidEye images were collected over forest of SPOT/VGT (path24/row24, September 30, 2010). We used Eq. (2) and Eq. (3) to calculate each of the RapidEye kernels. Input data for applying BRDF model are Table 3. We used Eq. (5) which is modified in Eq. (1), because BRDF parameters like as K_0 , K_1 and K_2 are difficult to directly calculate from high resolution satellites. Figure 14 and Figure 15 shown preliminary validation which is the SPOT/VGT K_0 and RapidEye K_0 . As previously mentioned, K_0 as the normalized reflectance is closely related to the BRDF parameters (isotropic value; K_0 , geometric value; K_1 , volumetric scattering value; K_2) and the kernels (geometric kernel; f_1 , volumetric scattering kernel; f_2). Figure 14 shows scatter plot of the SPOT/VGT and RapidEye K_0 relationship, and shows the linear relationship between the two. The R^2 value was 0.87 in Red band and 0.79 in NIR band. Figure 15 in the test area also shows the linear relationship between the two. The R^2 value was 0.74 in Red band and 0.65 in NIR band.

$$K_{0\text{SPOT/VGT}} = K_{0\text{RapidEye}} + \text{error} \quad (8)$$

RapidEye K_0 generally tended under-estimate, but we confirmed the linear relationship of the SPOT/VGT K_0 and RapidEye K_0 . Eq. (8) shows the SPOT/VGT and RapidEye K_0 simplified relationship. This mean that the RapidEye K_0 can be estimated from BRDF parameters of SPOT/VGT. Therefore, we performed error term analysis for directly estimating RapidEye K_0 .

Table 3. Input data of RapidEye to estimated geometric kernel and volumetric scattering kernel.

RapidEye	Study site	Test site
SZA (solar zenith angle)	38.4367°	38.22049°
VZA (viewing zenith angle)	0.1747°	0.1747°
SAA (solar azimuth angle)	178.10°	178.1215°
VAA (viewing azimuth angle)	279.77°	279.75°
f1 (geometric kernel)	-0.50614	-0.50224
f2 (volumetric scattering kernel)	-0.01770	-0.01761

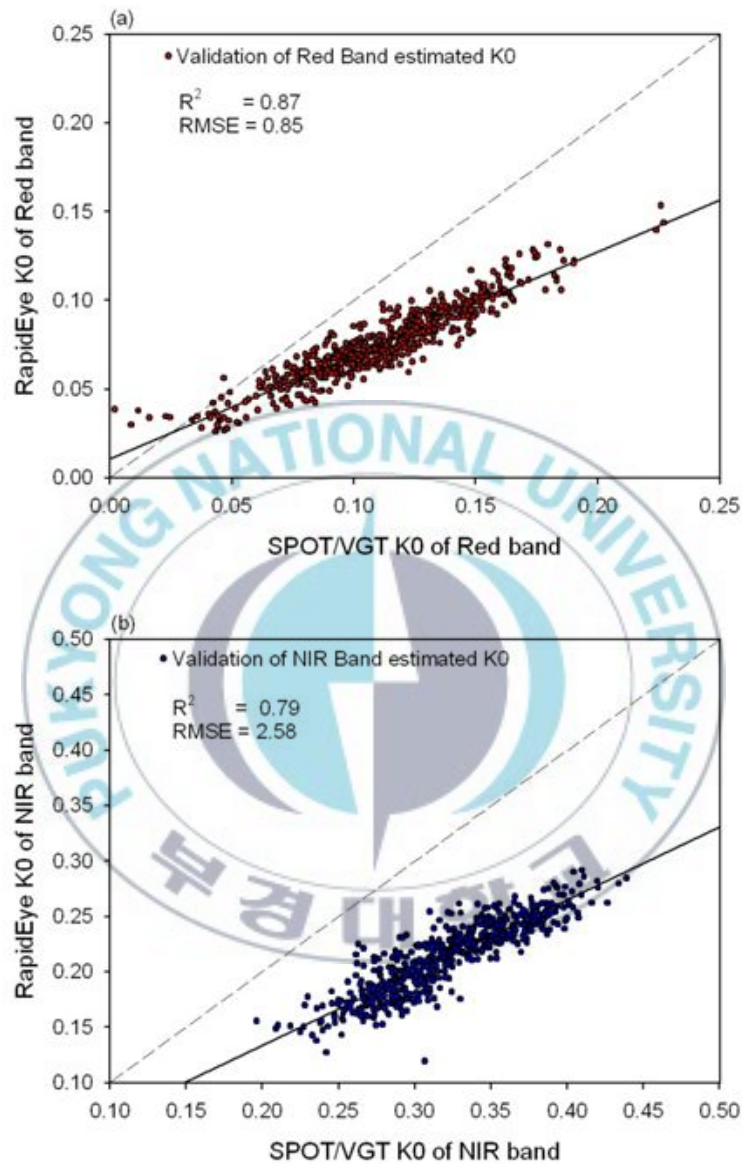


Figure 14. Preliminary validation of SPOT/VGT K0 and RapidEye K0 in the study area; (a) Red band; (b) Nir band

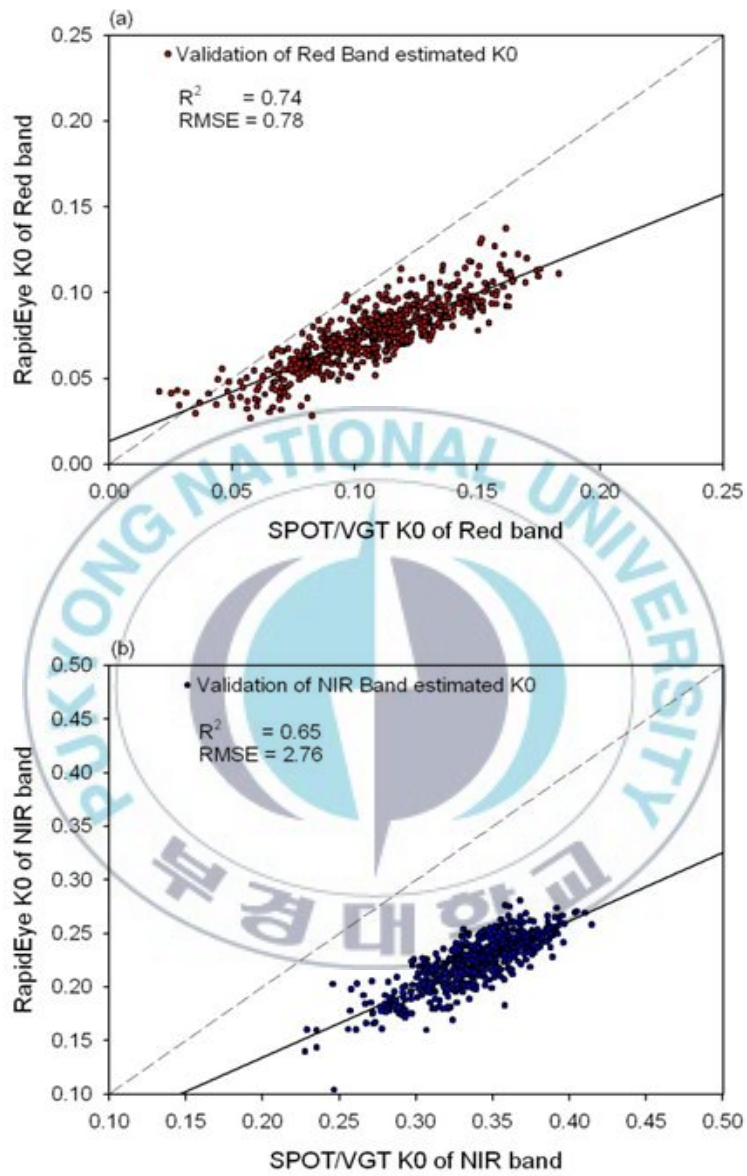


Figure 15. Preliminary validation of SPOT/VGT K0 and RapidEye K0 in the test area; (a) Red band; (b) Nir band

4.4.2. Comparison BRDF K_0 - adjusted weighting

Eq. (6) and Eq.(8) show the $K_{0\ SPOT/VGT} - \rho_{RapidEye}$, $-K_{1\ SPOT/VGT}f_{1\ RapidEye}$ and $-K_{2\ SPOT/VGT}f_{2\ RapidEye}$ terms corresponding to each channels ($K_{0\ SPOT/VGT} - \rho_{RapidEye}$ term; a dependent variable, $K_{0\ SPOT/VGT} - \rho_{RapidEye}$ and $-K_{2\ SPOT/VGT}f_{2\ RapidEye}$ term; the independent variables). Linear regression analysis was performed by using the parameters of SPOT/VGT like as isotropic value (K_0), geometric value (K_1) and volumetric scattering value (K_2), and the kernel values of RapidEye like as geometric kernel (f_1) and volumetric scattering kernel (f_2). Also it made a decision of weighting for K_1 , K_2 and error through regression models.

$$K_{0\ RapidEye} \quad (9)$$

$$= \rho_{RapidEye} + 1.506 K_{1\ SPOT/VGT}f_{1\ RapidEye} - 3.646 K_{2\ SPOT/VGT}f_{2\ RapidEye} + 0.018$$

$$K_{0\ RapidEye} \quad (10)$$

$$= \rho_{RapidEye} + 1.249 K_{1\ SPOT/VGT}f_{1\ RapidEye} - 0.983 K_{2\ SPOT/VGT}f_{2\ RapidEye} + 0.106$$

We estimated RapidEye K_0 about Red band using Eq. (9) and NIR band using the Eq. (10). The results of a correlation analysis between the SPOT/VGT K_0 and the applying weighted RapidEye K_0 , shown in Figure 16. Figure 16 shows that correlation existed ($R^2=0.89$, RMSE=0.002 in Red band, and $R^2=0.83$, RMSE=0.0006 in NIR band). To assess the accuracy of the weighting, we performed Eq. (9) and Eq. (10) over the test site. Figure 17 shows the result which is $R^2=0.83$, RMSE=0.09 in Red band, and $R^2=0.77$, RMSE=0.15 in NIR band. As a result, the weighting through linear regression analysis produced good agreement. For all sites, the SPOT/VGT K_0 and RapidEye K_0 had the high correlation (R^2 , RMSE), and generally were very consistent. We also compared with two area estimated to be using the weighting. Figure 18 shows a comparison between validation SPOT/VGT K_0 and RapidEye K_0 . Table 4 provides detailed information about the estimated RapidEye K_0 accuracies. The final estimated RapidEye K_0 was better than that in preliminary validation result, as supported by statistical results. Through weighted RapidEye K_0 by error term analysis, we estimated the the RapidEye K_0 directly using the SPOT/VGT. However, errors in the estimated the the RapidEye K_0 directly using the SPOT/VGT were observed without improved processing, and it was focused on some parts of the area. We also compared our results to those of other method (Figure19, 20). Figure 19 shown K_1 image applied weighting, K_2 image applied

weighting and estimated K_0 image over the study area. Figure 20 shown test area. Two values of K_1 and K_2 are in inverse proportion to each other. K_1 is in direct proportion to the estimated K_0 , and K_2 is in inverse proportion to the K_0 . K_0 seem to affects more K_2 values than K_1 values in the forest. In the future, we will apply weighting to various land cover about RapidEye reflectance.

Table 4. Result (R^2 and RMSE) of correlation analysis between SPOT/VGT and RapidEye about each of the channels

	RapidEye (Study area)		RapidEye (Test area)		Total	
	Red band	NIR band	Red band	NIR band	Red band	NIR band
R2	0.89	0.83	0.83	0.77	0.86	0.80
RMSE	0.0019	0.006	0.089	0.148	0.045	0.08

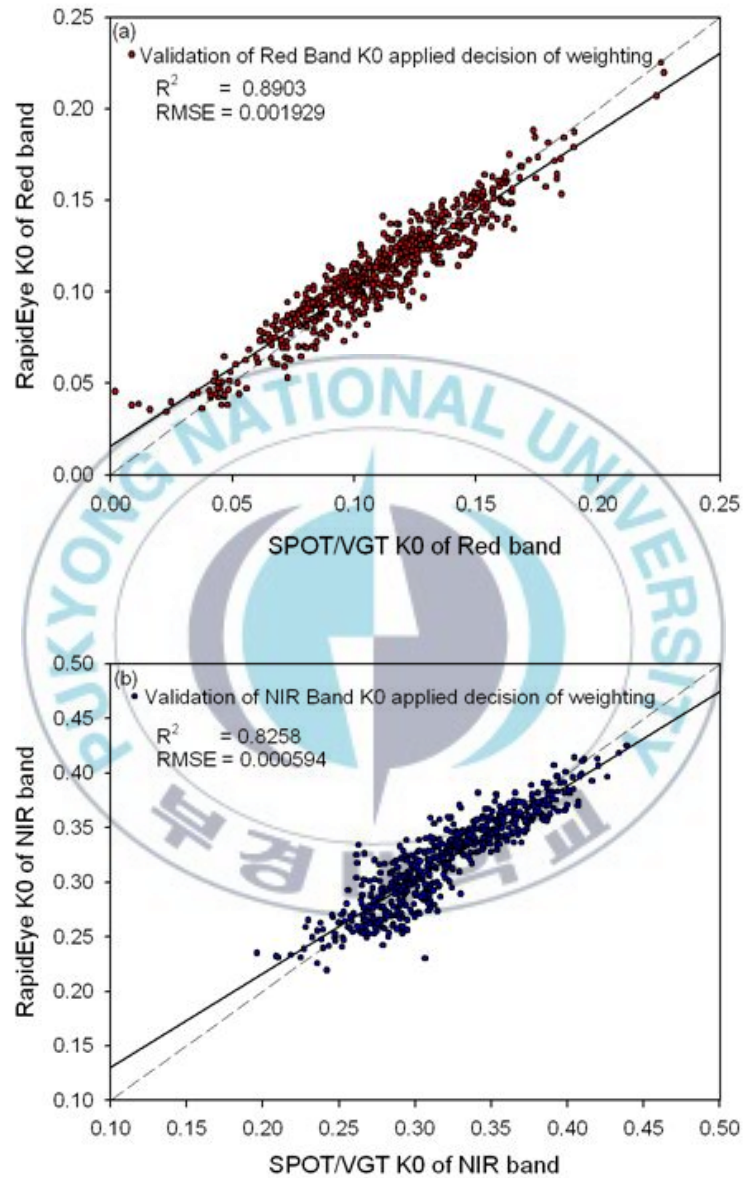


Figure 16. Validation of SPOT/VGT K0 and RapidEye K0-adjusted weighting K0 in the study area; (a) Red band; (b) Nir band

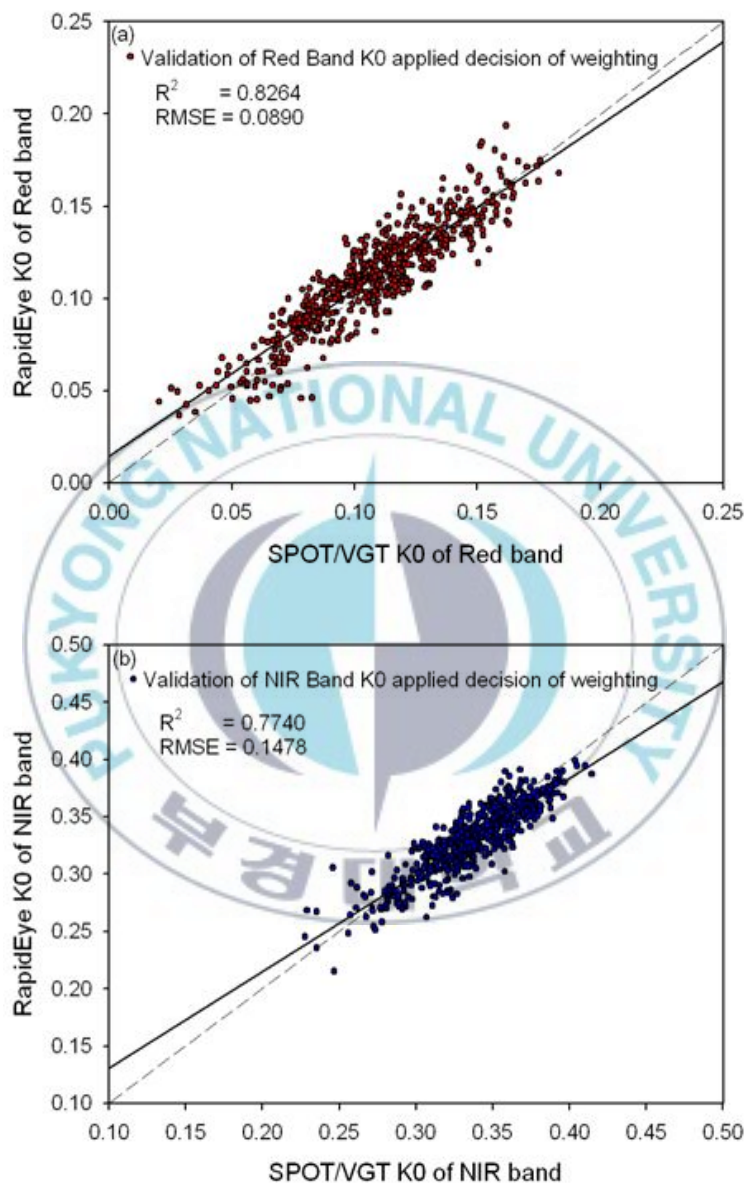


Figure 17. Validation of SPOT/VGT K0 and RapidEye K0-adjusted weighting K0 in the test area; (a) Red band; (b) Nir band

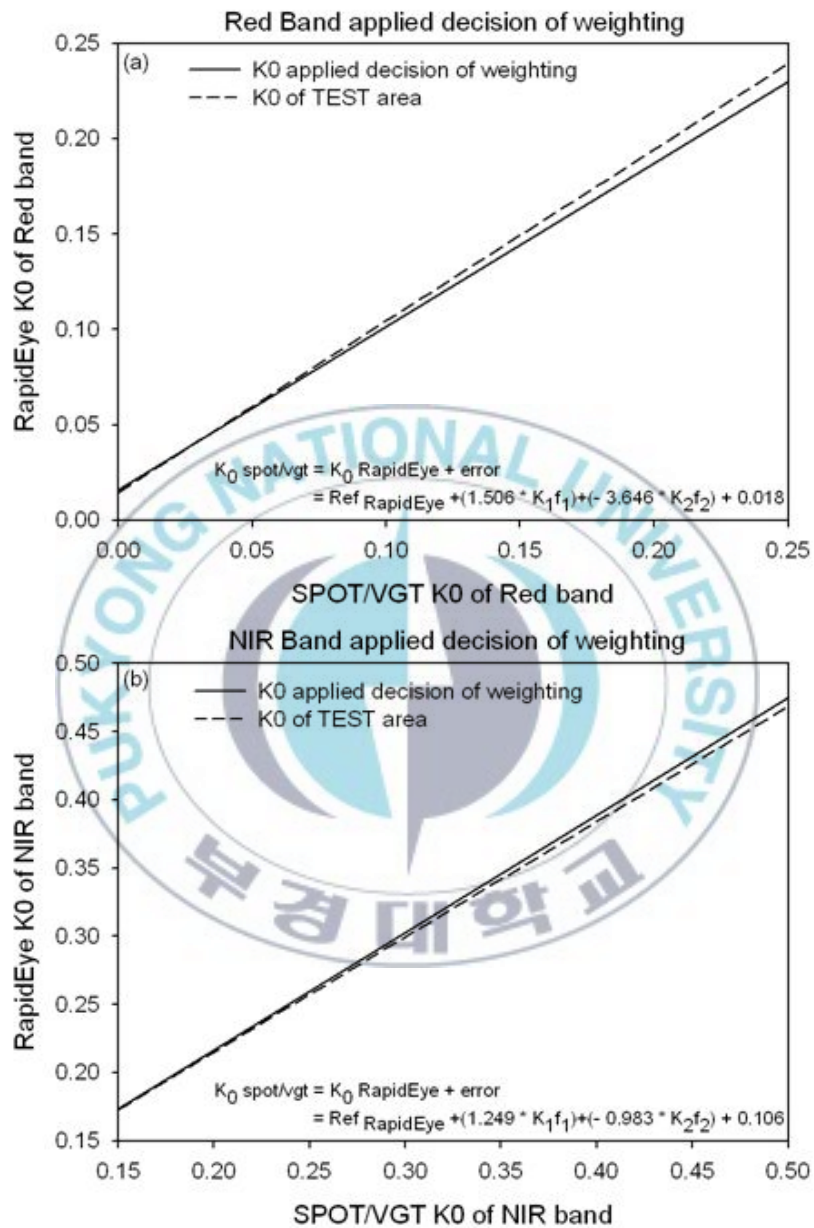
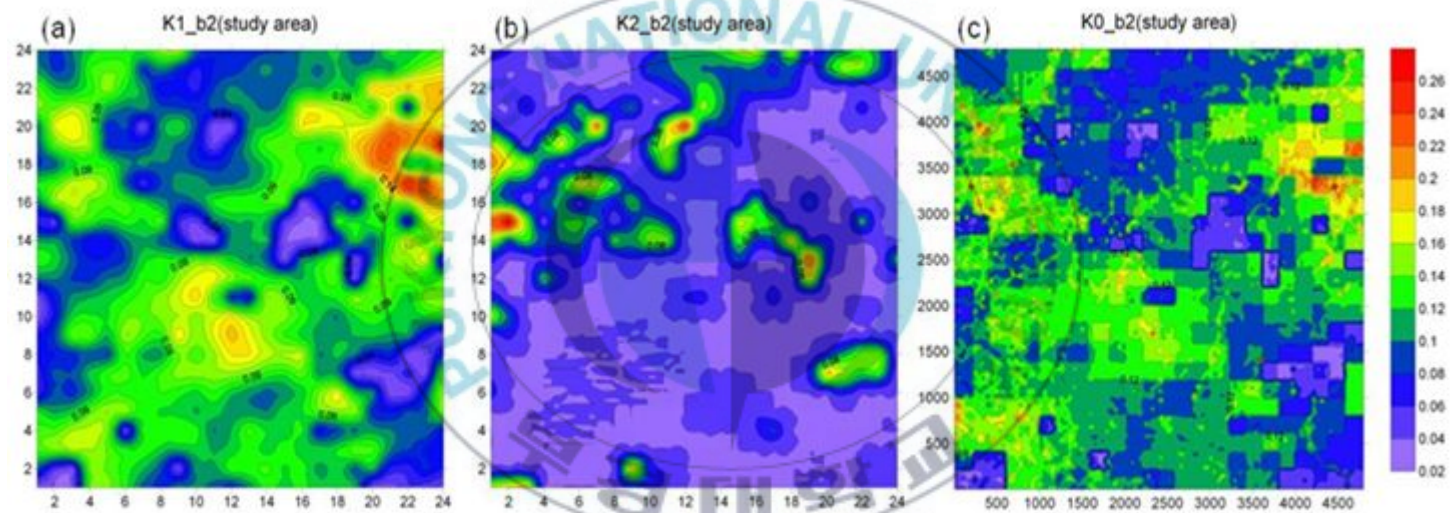


Figure 18. Comparisons of SPOT/VGT K0 and RapidEye K0-adjusted weighting K0 in the studyarea, and test area; (a) Red band; (b) Nir band



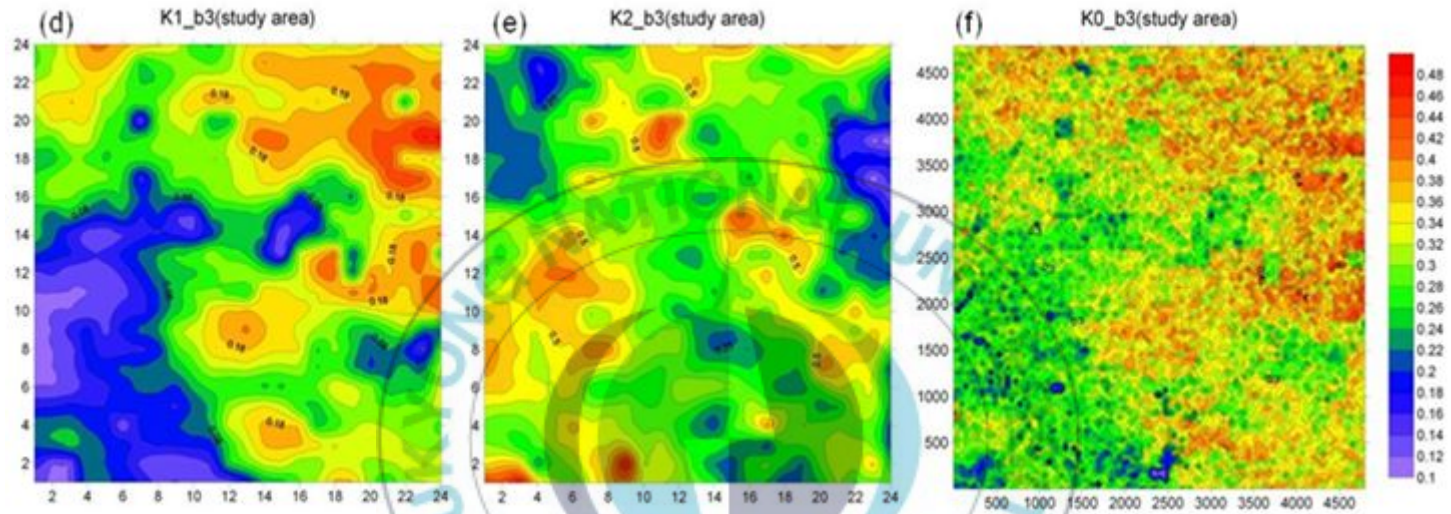
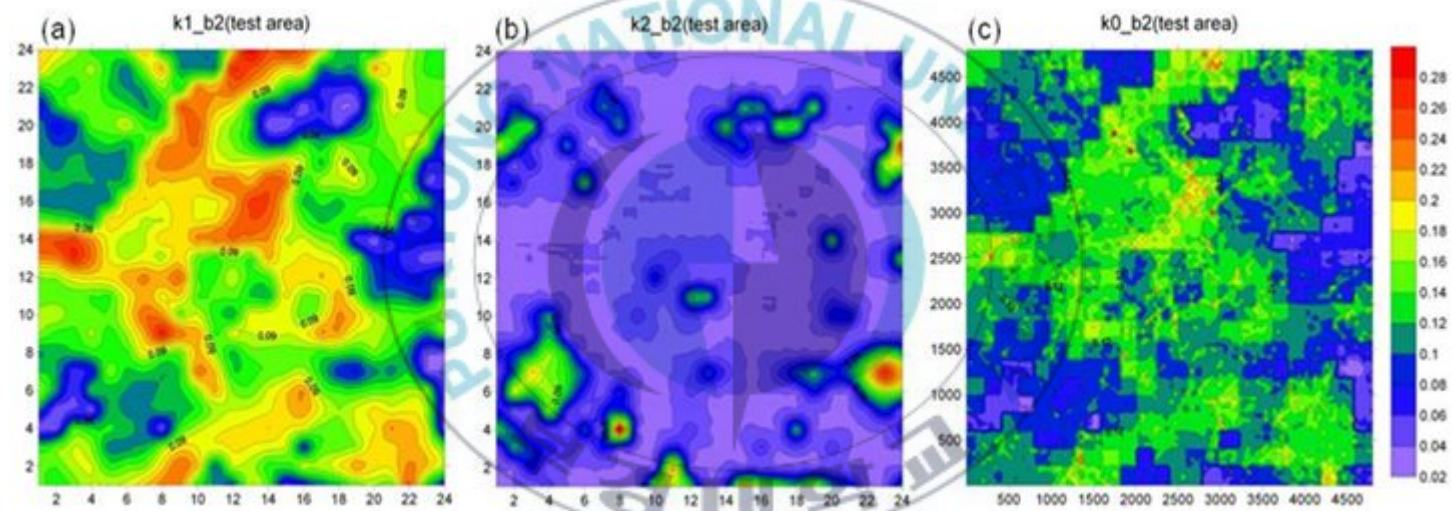


Figure 19. K1 image applied weighting, K2 image applied weighting and estimated K0 image over the study area: (a) red band of geometric value; (b) red band of volumetric scattering value; (c) red band of estimated isotropic value; (d) nir band of geometric value; (e) nir band of volumetric scattering value; (f) nir band of estimated isotropic value.



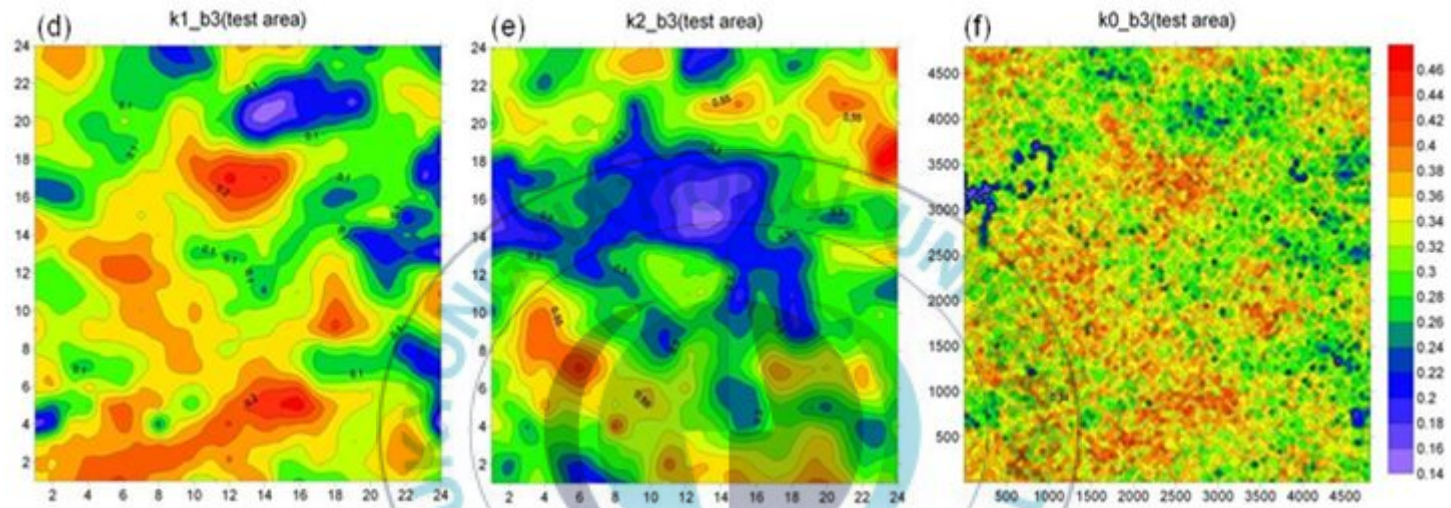


Figure 20. K1 image applied weighting, K2 image applied weighting and estimated K0 image over the test area: (a) red band of geometric value; (b) red band of volumetric scattering value; (c) red band of estimated isotropic value; (d) nir band of geometric value; (e) nir band of volumetric scattering value; (f) nir band of estimated isotropic value.

5. Conclusions

We used the method developed by Roujean, Leroy, and Deschamps (1992), considered to be the basic form for semi-empirical BRDF models. Also, we estimated geometric and volumetric term. When BRD effects are not eliminated, the reflectance is scattered randomly over the year. It is difficult to determine the representative temporal variation without consulting other information, to classify reflectance characteristic of surface changing according to the season (Jongmin Yeom et al., 2005). To extract geometric kernel and volumetric kernel, this study were performed to use B2 and B3 band that is useful for monitoring in growth of vegetation cover. The study is to understand surface reflectance anisotropy which is playing an important role in indicators of moisture and energy balance through land cover BRDF parameterization components. To add BRDF modeling of high resolution satellites which have insufficient angular samplings, this study identified BRDF components by extracting geometric and volumetric term from SPOT/VGT. Enhancement of f_1 depends on the azimuth angle, f_2 is less dependent on the azimuth angle. When was carried out comparison by land type, forest showed relatively larger value of geometric term than cropland. In other words, it was shown close relation about angle and NDVI value. In case of in cropland, the change of reflectance coefficient by band could not be almost

confirmed. However, in case of, the reflectance coefficient by band was difference according to the range of NDVI. Forest also showed tendency of similar distribution. NDVI above 0.6 showed similarity that is the increasing B3 band values over the cropland and forest.

We tested the performance of the SPOT/VGT BRDF components when estimated RapidEye K_0 . Typically, the wide swath satellites like SPOT/VGT permit sufficient angular sampling, but high resolution satellites are impossible to obtain sufficient angular sampling over a pixel during short period because of their narrow swath scanning and VZA (Viewing Zenith Angle) range within the range $0\sim5^\circ$. Consequently, BRDF parameters are difficult to directly calculate from high resolution satellites. To solve this problem, we performed linear regression analysis by using the parameters of SPOT/VGT like as isotropic value (K_0), geometric value (K_1) and volumetric scattering value (K_2), and the kernel values of RapidEye like as geometric kernel (f_1) and volumetric scattering kernel (f_2). Also it made a decision of weighting for K_1 , K_2 and error through regression models. We compared the SPOT/VGT K_0 estimates with validation RapidEye K_0 to assess their accuracy. Correlation existed ($=0.89$, $RMSE=0.002$ in Red band, and $R^2=0.83$, $RMSE=0.0006$ in NIR band). To assess the accuracy of the weighting, test site shows the result which is $R^2=0.83$, $RMSE=0.09$ in Red band, and $R^2=0.77$, $RMSE=0.15$ in NIR

band. As a result, the weighting through linear regression analysis produced good agreement. For all sites, the SPOT/VGT K_0 and RapidEye K_0 had the high correlation (R^2 , RMSE), and generally were very consistent. We also compared with two area estimated to be using the weighting. However, this study has several limitations in simple comparison about reflectance of RapidEye and SPOT/VGT, and in efficiency assessment test. In the future, this researcher will be utilized as basic data for estimating normalized reflectance of high resolution satellite and we will apply weighting to various land cover about RapidEye reflectance.



6. REFERENCE

- Chopping, M. J., 2000. Testing a LiSK BRDF model with in situ bidirectional reflectance factor measurements over semiarid grasslands. *Remote Sensing of Environment*, 74: 287-312.
- Csiszar, I., G. Gutman, P. Romanov, M. Leroy, and O. Hautecoeur, 2001. Using ADEOS/POLDER data to reduce angular variability of NOAA/AVHRR reflectances. *Remote Sensing of Environment*, 76: 399-409.
- Dickinson, R. E. 1983. Land surface processes and climate surface albedos and energy balance. *Advances in Geophysics*, 25, 305-353.
- Duchemin, B. and P. Maisongrande, 2002. Normalization of directional effects in 10-day global syntheses derived from VEGETATION/SPOT: I. Investigation of concepts based on simulation. *Remote Sensing of Environment*, 81: 90-100.
- Gao, W., 1993. A simple bidirectional-reflectance model applied to a tallgrass canopy. *Remote Sensing of Environment*, 45: 209-224.
- Han, K. S., J. L. Champeaux, J. L. Roujean, 2004, A land cover classification product over France at 1 km resolution using SPOT4/VEGETATION data. *Remote Sensing of Environment*,

92(1): 52-66.

Hartigan and Wong, 1979 J.A. Hartigan and M.A. Wong, A k-means clustering algorithm. Algorithm AS136, Appl. Stat. 28, pp. 100–108.

Hu, B., W. Wanner, X. Li, and A. H. Strahler, 1997. Validation of kernel-driven semi-empirical models for global modeling of bidirectional reflectance. *Remote Sensing of Environment*, 62: 201– 214.

Jang, J. D., and A. A. Viau, 2004. Neural network estimation of air temperatures from AVHRR data, *International Journal of Remote Sensing*, 24(21):4541-4554.

Jensen, J.R., 1994. In: *Introductory digital image processing: A remote sensing perspective*, Prentice Hall, New Jersey, USA, p. 316.

Jiang, Z., A. R. Huete, J. Chen, Y. Chen, Li, G. Yan and X. Zhang, 2006. Analysis of NDVI and scaled difference vegetation index retrievals of vegetation fraction. *Remote Sensing of Environment*, 101(3): 366-378.

Kimes, D. S., W. W. Newcombe, C. J. Tucker, I. W. Zonnefeld, W. van Vijingaarden, J. de Leeuw, and G. F. Epema, 1985. Directional reflectance factor distributions for cover types of Northern Africa. *Remote Sensing of Environment*, 18: 1-19.

King, M. D., Y. J. Kaufman, W. P. Menzel, and D. Tanre, 1992. Remote sensing of cloud, aerosol, and water vapor properties from the Moderate Resolution Imaging Spectrometer (MODIS), IEEE

- Transactions on Geoscience and Remote Sensing, 30(1):2-27.
- Lacaze, R., and J. L. Roujean, 2001. G-function and HOT SPOT (GHOST) reflectance model application to multi-scale airborne POLDER measurements. *Remote Sensing of Environment*, 76: 67– 80.
- Lucht, W., C. B. Schaaf, and A. H. Strahler, 2000. An algorithm for the retrieval of albedo from space using semiempirical BRDF models. *IEEE Transactions on Geoscience and Remote Sensing*, 38: 977– 998.
- Passot, X., 2000. VEGETATION image processing methods in th CTIV, *In vegetation 2000, 2 years of operation to prepare the future (Belgirate, Italy: The european commission)*, 15-22.
- Pinty, B., and M. M. Verstraete, 1991. Extracting information on surfaceproperties from bidirectional reflectance measurements. *Journal of Geophysical Research*, 96: 2865– 2879.
- Pokrovsky, O., and J. L. Roujean, 2002. Land surface albedo retrieval via kernel-based BRDF modeling: II. An optimal design scheme for the angular sampling. *Remote Sensing of Environment*, 84: 120-142.
- Privette, J. L., T. F. Eck, and D. W. Deering, 1997. Estimating spectral albedo and nadir reflectance through inversion of simple BRDF models with AVHRR/ MODIS-like data. *Journal of*

Geophysical Research, 102: 29529– 29542.

Roujean, J. L, M. Leroy, and P. Y. Deschamps, 1992. A bidirectional reflectance model of the earth's surface for the correction of remote sensing data. *Journal of Geophysical Research*, 97(D18): 20455-20468.

Tarpley, J. D., S. R. Schneider, and R. L. Money, 1984. Global vegetation indices from the NOAA-7 meteorological satellite. *Journal of Applied Meteorology*, 23: 491-494.

Walthall, C. L., 1985. A study of reflectance anisotropy and canopy structure using a simple empirical model. *Remote Sensing of Environment*, 61: 118-128.

Wanner, W., and A. H. Strahler, 1995. On the derivation of kernels for kernel-driven models of bidirectional reflectance. *Journal of Geophysical Research*, 100: 21077–21089.

Xiao, X., D. Hollinger, J. D., Aber, M. Goltz, E. A. Davidson, and Q. Y. Zhang, 2004a. Satellite-based modeling of gross primary production in an evergreen needleleaf forest, *Remote Sensing of Environment*, 89(4):519-534.

Xiao, X., Q. Zhang, B. Braswell, S. Urbanski, S. Boles, S. Wofsy, B. Moore III, D. Ojima, 2004b. Modeling gross primary production of temperate deciduous broadleaf forest using satellite images and climate data, *Remote Sensing of Environment*, 91(2):256-270.

Yeom, J. M., K. S. Han, and Y. S. Kim, 2005. A Reflectance Normalization

Via BRDF Model for the Korean Vegetation using MODIS 250m Data . *Korean Journal of Remote Sensing*, Vol.21, No.6, 361-368

Yeom, J. M., K. S. Han, 2009. An Efficiency Analysis for Data Synthesis of Sun- and Geo-Synchronous Satellites in kernel-driven BRDF Model. *Asia-Pacific Journal of Atmospheric Sciences*, 45, 4, 499-511

Zhuosen, W., S. Crystal B., L. Philip , K. Yuri, S. Mitchell A., S. Alan H., Y. Tian, M. Ranga B., C. Mark J., B. Bryan J., 2011. Retrieval of canopy height using moderate-resolution imaging spectroradiometer (MODIS) data. *Remote Sensing of Environment*, 115: 1595–1601.

